Henrik Tydesjö

Net-Charge Fluctuations in Ultra-Relativistic Nucleus-Nucleus Collisions

Department of Physics
Lund University
2004

Net-Charge Fluctuations in Ultra-Relativistic Nucleus-Nucleus Collisions

Henrik Tydesjö
Department of Physics
Lund University, Sweden

To be presented with the permission of the Faculty of Natural Sciences of Lund University, for public criticism in lecture hall B at the Department of Physics on October 7 2004, at 13.15.

Organization
LUND UNIVERSITY
Department of Physics
Box 118
SE-221 00 LUND
SWEDEN

Document name
DOCTORAL DISSERTATION

Date of issue
August 23, 2004

Sponsoring organization

Author(s)
Henrik Tydesjö

Title and subtitle
Net-Charge Fluctuations in Ultra-Relativistic Nucleus-Nucleus Collisions

Abstract

PHENIX is one of four experiments at the Relativistic Heavy-Ion Collider, RHIC. The high-energy heavy-ion collisions provided by this accelerator offer the possibility to study nuclear matter at high temperature and density. The high multiplicity of particles produced in these collisions puts high demands on detector performance. Providing space points along particle trajectories, the Pad Chamber detector system in PHENIX gives valuable information for charged particle tracking at midrapidity.

In the collisions, nuclear matter is believed to undergo a phase transition to a state called the Quark-Gluon Plasma (QGP). In this state, quarks and gluons are not confined inside the hadrons, as in ordinary nuclear matter. In the search for such a deconfined phase, a lot of signatures has been suggested. One of those is based on information about the event-by-event net-charge fluctuations. These fluctuations have been studied in PHENIX at two different beam energies.

Key words: Heavy-Ion Collisions, RHIC, PHENIX, Quark-Gluon Plasma, Net-Charge Fluctuations, Pad Chamber

Classification system and/or index termes (if any):

Supplementary bibliographical information:

Language
English

ISSN and key title:

ISBN
91-628-6217-0

Recipient's notes

Number of pages
150

Price

Security classification

Popularised Summary in Swedish

Denna avhandling grundar sig på forskning inom fältet "högenergetisk tungjonsfysik", där man studerar materia under extrema förhållanden vad gäller temperatur och densitet. Experimenten utförs på stora anläggningar där atomkärnor accelereras till höga hastigheter innan de kolliderar med varandra. Höga krav ställs på de partikeldetektorer som byggs upp kring sådana interaktionspunkter i syfte att registrera vad som händer vid kollisionerna.

Det primära målet med forskningen är att upptäcka och studera det materietillstånd som fått benämningen kvark-gluonplasma (QGP, efter engelskans Quark-Gluon Plasma). Universums materia antas ha befunnit sig i detta tillstånd ögonblicken efter Big Bang. Tillståndet kännetecknas av att kvarkarna och gluonerna, som normalt är bundna inne i protoner och neutroner, kan röra sig fritt i en större volym. Genom högenergetiska tungjonskollisioner tror man sig kunna skapa så hög temperatur och densitet att man får en s.k. fasövergång till detta materietillstånd. Det har dock visat sig vara besvärligt att hitta tillförlitliga signaler som tyder på att en fasövergång ägt rum. En av de grundläggande svårigheterna är tillståndets korta livstid.

I avhandlingen beskrivs PHENIX-experimentet, som är ett av fyra experiment vid acceleratorn RHIC (Relativistic Heavy-Ion Collider) på Brookhaven National Lab i USA. Här har man under olika perioder sedan år 2000 kolliderat guldkärnor vid olika kollisonsenergier. (Även kollisioner mellan protoner och mellan deuteroner och guldkärnor har studerats.) Forskargruppen från Lund har lagt stort arbete på ett specifikt detektorsystem, de s.k. padkamrarna. Dessa detektorer består av gasfyllda kammare som registrerar passagen av laddade partiklar. Dessa detektorer uppvisar hög effektivitet och god positionsupplösning.

År 1999 presenterades idén till en analysmetod som skulle kunna fungera som en signal för att QGP skapats. Den grundar sig på att fördelningen av elektrisk

laddning i ett QGP är jämnare än i normal s.k. hadronisk materia. Detta beror på att laddningsbärarna i QGP, kvarkarna, bär laddningar om $\pm 1/3$ eller $\pm 2/3$, d.v.s. lägre än enhetsladdningen. Det finns alltså 2-3 gånger fler laddningsbärare i QGP än i hadronisk materia, därav en jämnare fördelning. Det antogs att denna effekt skulle bevaras även efter att plasmat hadroniserat, så att man i ett experiment skulle kunna uppmäta en minskning av lokala fluktuationer i nettoladdningen. De första analyserna av sådana fluktuationer från PHENIX-experimentet presenteras i denna avhandling.

Contents

Preface

The work that this thesis is based on has been carried out both at my home institution at Lund University, and at Brookhaven National Lab (BNL) in USA. The Lund research group is involved in PHENIX, which is one of four experiments at the Relativistic Heavy-Ion Collider (RHIC) at BNL.

In this thesis an introduction to the field of high-energy heavy-ion physics is given. The PHENIX experiment is described, with some emphasis on the pad chamber detectors. Much of my work has been concentrated on software connected to these detectors (hit reconstruction, detector response simulation, high-voltage settings, online monitoring of performance, calibration etc.). Finally, the thesis describes the specific topic I have focused on; Net-Charge Fluctuations. The analysis work in PHENIX led to the publication of PAPER III. The data presented here were taken in year 2000 for collisions of gold nuclei at a beam energy of 65+65 GeV/nucleon. An analysis of the 100+100 GeV/nucleon data from year 2002 has just been finished and the first results are presented here.

A list of the papers included in this thesis is given on page xi.

Paper I gives a description of the event reconstruction techniques used in the PHENIX central arm spectrometers. An introduction to the nine detector subsystems is given, along with a description of the specific information they provide. It is explained how this information is put together for charged particle tracking, momentum reconstruction, and particle identification.

Paper II describes the Pad Chamber detector system in the PHENIX experiment. These detectors are placed in layers and provide space points along particle trajectories, altogether covering an area of 88 m^2. To fulfill all operational requirements a unique design of these wire chambers was invented. The detectors are read out on their finely segmented cathode planes via electronics mounted directly onto the face of the chambers. Results on efficiency and position resolution measurements, using cosmic rays, are presented.

Paper III presents results on net-charge fluctuations in gold-gold collisions in PHENIX at $\sqrt{s_{NN}} = 130$ GeV. The measured fluctuations are somewhat reduced compared to a pure global charge conservation scenario. The reduction is consistent with a resonance gas prediction, but not large enough for the quark-gluon plasma prediction as claimed by some of the pioneering theories on this physics topic.

Paper IV utilizes a simulation tool developed to get information on how various net-charge fluctuation measures behave in different experimental scenarios. Simple models of charged particle production via resonance decays and hadronization from a quark-gluon plasma are tested. The results show that the fluctuation measures are strongly influenced by correlations between positive and negative particles, as generated in these models.

Henrik Tydesjö, July 2004

List of Included Papers

I J.T. Mitchell *et al.*
Event reconstruction in the PHENIX central arm spectrometers
Nucl. Instr. and Methods A **482** (2002) 491

II K. Adcox *et al.*
Construction and performance of the PHENIX pad chambers
Nucl. Instr. and Methods A **497** (2003) 263

III K. Adcox *et al.* (PHENIX collaboration).
Net Charge Fluctuations in Au + Au Interactions at $\sqrt{s_{NN}} = 130$ GeV
Physical Review Letters **89** (2002) 082301

IV J. Nystrand, E. Stenlund, and H. Tydesjö
Net-charge fluctuations in relativistic heavy-ion interactions
Physical Review C **68** (2003) 034902

The papers are reprinted with the permission of the copyright holders, Elsevier Science (papers I and II) and the American Physical Society (papers III and IV). Their cooperation is gratefully acknowledged.

Chapter 1

High-Energy Heavy-Ion Physics

1.1 The Beginning

According to current theories of cosmic evolution, the universe began with a singular explosion. After this so-called Big Bang the conditions of the universe were so extreme that phases of matter, not observed today, were formed. As the universe expanded and cooled, transitions took place as matter changed from one phase to another, like steam condensing into water. One of these transitions, called the quark-gluon plasma phase transition, took place only microseconds after the Big Bang.

1.2 The Quark-Gluon Plasma

Quarks, along with *leptons*, are the fundamental constituents of matter. In the standard model [1] there are six quark flavors, arranged in three families, as illustrated in figure 1.1.

$$\begin{pmatrix} u \\ d \end{pmatrix} \begin{pmatrix} c \\ s \end{pmatrix} \begin{pmatrix} t \\ b \end{pmatrix}$$

Figure 1.1: The quarks are called up, down, charm, strange, top and bottom. For each flavor there is also a corresponding anti-quark. The top row has electric charge $q = \frac{2}{3}e$ and the bottom row has $q = -\frac{1}{3}e$, where e is the charge unit, i.e. the electric charge of the electron.

Quantum Chromo Dynamics [2], QCD, is the quantum field theory that best describes the strong interaction between the quarks and the gluons. The

attractive force between quarks grows rapidly for large separations ($\gtrsim$ 1 fm), confining them into hadrons. The quarks are fermions and have to obey the Pauli principle, and to account for all known hadrons, QCD introduces a quantum property called color charge. Each quark (anti-quark) is assigned a color of red, green or blue (anti-red, anti-green, anti-blue). Only color neutral objects are allowed. The mesons consist of two quarks ($q_{color}\overline{q}_{\overline{color}}$), while the baryons consist of three ($q_{red}q_{green}q_{blue}$ or $\overline{q}_{\overline{red}}\overline{q}_{\overline{green}}\overline{q}_{\overline{blue}}$).

The *gluons* are the exchange particles of the strong interaction. Since they – themselves – carry color charge, they couple not only to quarks but also to each other. This fact can be shown to imply a property called "asymptotic freedom", which means that the interaction gets weaker at short distances ($\lesssim$ 1 fm). At large baryon densities (substantially larger than for ground state nuclei) and high temperatures, nuclear matter is therefore expected to undergo a phase transition to a state called the *quark-gluon plasma*, QGP [3, 4]. In this state, the quarks are not confined to the hadrons. Quarks and gluons instead move over the whole, high-density system. Besides this *deconfinement*, *chiral*

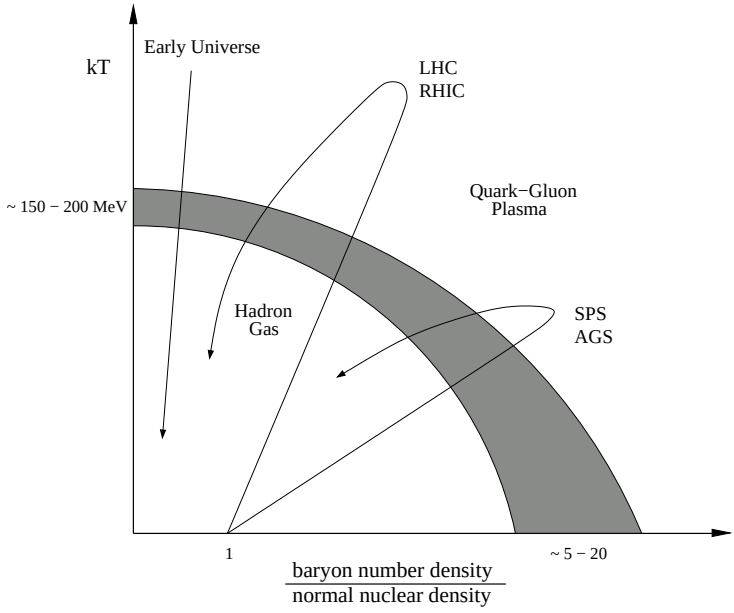

Figure 1.2: QCD phase diagram. Lattice calculations at low baryon densities predict a phase transition at a temperature of about 150-200 MeV.

symmetry is expected to be restored in a QGP, which means that the quark masses will approach zero.

A predicted phase diagram of nuclear matter is shown in figure 1.2. The increase in available energy in the collisions when going from SPS to LHC, results in a higher temperature and more baryon free region. Approaching the conditions prevailing in the early universe, there is however one major difference. The time scale at which the phase transition takes place is $\sim 10^{-22}$ s for heavy-ion collisions, while for the Big Bang scenario it is ~ 10 μs. A QGP may today exist in the core of very dense neutron stars, at large baryon density in the lower right region of the phase diagram.

Accelerators designed to provide high-energy heavy-ion collisions offer a possible way to create and study the QGP. The collisions produce a hot and dense system that may reach energy densities and temperatures high enough for a phase transition to occur. The remaining sections of this chapter describe such experimental facilities and the physics that can be extracted from them.

1.3 Experimental Facilities

Table 1.1 summarizes the development of heavy-ion accelerators. The first

Accelerator	*Beams*	$\sqrt{s_{NN}}$ *[GeV]*	*Startup year*
AGS, BNL	^{16}O,^{28}Si	5.4	1986
	^{197}Au	4.9	1992
SPS, CERN	^{16}O,^{32}S	19.4	1986
	^{208}Pb	17.3	1994
RHIC, BNL	^{197}Au	130	2000
		200	2001
		62.5	2004
LHC, CERN	^{208}Pb	5 500	2007

Table 1.1: Heavy-ion accelerators described in terms of accelerated nuclei and available energy.

generation of accelerators were *fixed-target* machines, where the beam of ions is accelerated to the operating energy and then extracted and steered on to a stationary target. In *collider* machines, two beams traveling in opposite directions are brought to collide, making all the kinetic beam energy available for production of new particles.

The only operational heavy-ion collider is the *Relativistic Heavy-Ion Collider*, RHIC [5], at Brookhaven National Laboratory located on Long Island, New York. RHIC is capable of colliding a wide variety of particle species from gold nuclei to polarized protons. With a circumference of about 3.8 km the RHIC ring accelerates gold ions to 99.995% the speed of light, corresponding to an energy of 100 GeV per nucleon.

There are four experiments located at different interaction points along the RHIC ring: PHOBOS, BRAHMS, STAR and PHENIX. The Au+Au collisions at these points produce thousands of particles, requiring high granularity detectors. The different detectors used in the experiments are designed to perform certain types of measurements, each important for the understanding of the physics involved in the collisions. The PHENIX experiment [6] will be described in detail in chapter 2.

The *Large Hadron Collider*, LHC, is now under construction at CERN. There will be one dedicated heavy-ion experiment named ALICE. The first heavy-ion run at LHC is scheduled for 2007.

1.4 Collision Characteristics

The *spectator-participant model* [7] of a heavy-ion collision is illustrated in figure 1.3. The participating nucleons from overlapping nuclear parts create a volume of high temperature and density, while the spectators move basically undisturbed through the collision. The impact parameter b determines the *centrality* of the collision. The impact parameter is not directly measurable in the collisions. To determine the collision geometry, measurements of quantities which are strongly correlated to the number of participants are used, such as the transverse and forward energy and the number of produced particles. The transverse energy, E_T, is defined as

$$E_T = c^2 \sum_{i=1}^{N} (m_T)_i \tag{1.1}$$

where i runs over all N particles and the transverse mass m_T is given by

$$m_T = \sqrt{m^2 + (p_T/c)^2} \tag{1.2}$$

where p_T is the momentum component perpendicular to the beam direction. In practice, E_T is measured with a segmented calorimeter, and calculated as the sum of the energy E_i at polar angle θ_i in each segment (i):

$$E_T = \sum_{i=1}^{N} E_i \cdot \sin\theta_i \tag{1.3}$$

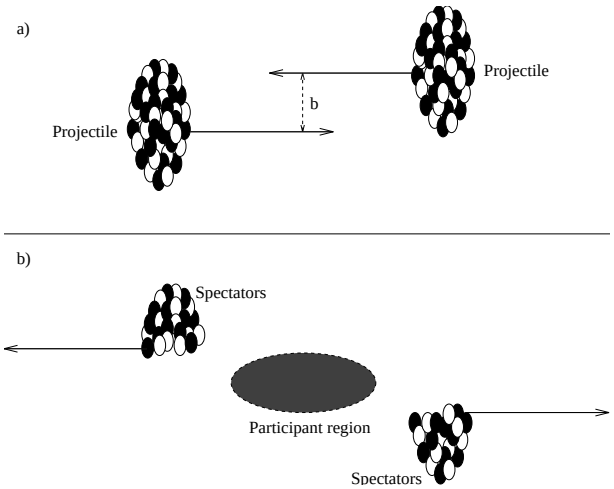

Figure 1.3: A collision between two heavy nuclei in the spectator-participant model.
a) The two Lorentz contracted nuclei before the collision. The centrality is determined by the impact parameter b.
b) After the collision a participant region with high temperature and density is created.

Instead of the velocity v of a particle, it is often more convenient to use a quantity called *rapidity*, defined by

$$y = \operatorname{arctanh}\left(\frac{v}{c}\right) \tag{1.4}$$

The rapidity is additive also in the relativistic case. In heavy-ion collision terminology the rapidity is measured along the beam direction (z). An equivalent definition is then given by

$$y = \frac{1}{2}\ln\frac{E + p_z c}{E - p_z c} \tag{1.5}$$

where E is the energy of the particle and p_z its momentum component along the beam direction. A frequently used approximation to the rapidity is the *pseudo-rapidity*,

$$\eta = -\ln\left(\tan\frac{\theta}{2}\right) \tag{1.6}$$

Here θ is the polar emission angle, i.e. the angle between the particle momentum $\vec{p}$ and the beam axis. Expressed in terms of momentum, the pseudo-rapidity is

$$\eta = \frac{1}{2}\ln\left(\frac{|\vec{p}| + p_z}{|\vec{p}| - p_z}\right) \tag{1.7}$$

and the exact relation between the rapidity and the pseudo-rapidity is

$$\sinh \eta = \frac{m_T \cdot c}{p_T} \sinh y \tag{1.8}$$

The pseudo-rapidity approximation is good at large transverse momenta ($p_T \gg mc$).

1.5 Thermodynamic Properties

Since heavy-ion collisions produce a very high multiplicity of particles, a statistical treatment of the system can be adopted. If thermal equilibrium is reached, the system can be characterized by thermodynamic observables, such as volume, temperature, energy density and entropy density.

The expected space-time evolution of a heavy-ion collision - with and without QGP formation - is sketched in figure 1.4.

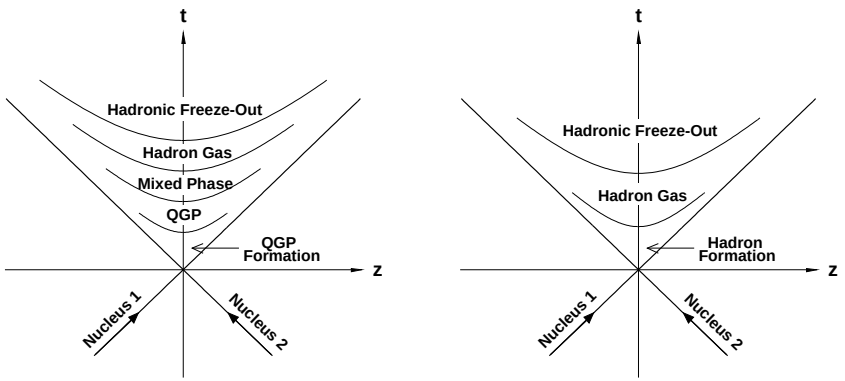

Figure 1.4: A collision between two heavy nuclei takes place at $(z,t) = (0,0)$ where z is the space coordinate along the beam axis and t is the time coordinate. The figures indicate the evolution of the system with QGP formation (left), and without QGP formation (right). The hyperbolae are constant proper-time curves, where the proper-time $\tau = \sqrt{t^2 - z^2}$ (c=1). In the hydrodynamic model described in [3] the energy density, entropy density and temperature are constant on each curve. The time-scale is on the order of a few fm/c.

Identical-particle interferometry, also referred to as HBT (Hanbury-Brown-Twiss) correlations [8], e.g. $\pi\pi$ or KK correlations, can be used to study the space-time dynamics of nuclear collisions. From such two-particle correlations

it is in principle possible to obtain information on the transverse and longitudinal size, on the lifetime and on flow patterns of the source at the freeze-out time. For instance, different particle species may freeze out at different times and give different source sizes, due to the expansion of the source. Similar information can be obtained by analyzing the coalescence of e.g. (anti)protons and (anti)neutrons into (anti)deuterons, as in [9].

With a hydrodynamic description of the colliding system, as in [3], the energy density ϵ can be estimated from the transverse energy per unit rapidity as [1]

$$\epsilon = \frac{1}{V}\frac{dE_T}{dy} = \frac{1}{\tau_0 \pi R^2}\frac{dE_T}{dy} \tag{1.9}$$

Here R is the transverse radius of the participant zone and τ_0 is the proper formation time. Usually a value of $\tau_0 = 1$ fm/c is used.

The particle emission from a source in thermal equilibrium is Maxwell-Boltzmann distributed according to [10]

$$\frac{dN}{m_T dm_T} \propto m_T K_1 \left(m_T/T\right) \tag{1.10}$$

where K_1 is the modified Bessel function

$$K_1(m_T/T) = \int \cosh(y) e^{-m_T \cosh(y)/T} dy \tag{1.11}$$

For full rapidity coverage and with the assumption that $m_T \gg T$ equation 1.10 can be approximated as

$$\frac{dN}{m_T dm_T} \propto \sqrt{m_T} e^{-m_T/T} \tag{1.12}$$

For a narrow rapidity window, the approximation is

$$\frac{dN}{m_T dm_T} \propto e^{-m_T/T} \tag{1.13}$$

The temperature would then be given by the inverse slope of a semilogarithmic diagram of $1/m_T \cdot dN/dm_T$ versus m_T.

1.6 Quark-Gluon Plasma Signatures

Quarks and gluons coexisting in the short-lived QGP state cannot be measured directly, and information from the early stages of the collision may get lost when the system hadronizes. The various kinds of measurements suggested probably have to be combined to get reliable proof of the formation of a QGP. A description of the ideas behind some of the most promising signatures is given below.

[1] In the original paper an error of a factor 1/2 appears.

Jet Quenching

The propagation of partons through a hot and dense medium modifies their transverse momentum due to induced radiative energy loss, a phenomenon called *jet quenching* [11, 12]. This can be studied by measuring the p_T distribution of hadrons coming from high-p_T jets.

When a hard collision, producing two jets, occurs near the surface of the nuclear overlap region, jet quenching might lead to complete absorption of one of the jets, while the other escapes. This signature can be found by studying azimuthal back-to-back correlations of jets.

In general, high-p_T partons traveling through the dense medium is probably one of the best probes that can be used to characterize the medium. Studying the thereby produced particles, correlated in transverse momentum and emission angle, is often referred to as jet tomography.

In a series of papers, PHENIX reports a suppression of high-p_T hadrons in central Au-Au collisions, as compared to p-p and d-Au collisions [13, 14, 15, 16]. STAR has also measured a suppression in the high-p_T hadron yield, as well as a clear suppression of back-to-back jet correlations in central Au-Au collisions compared to p-p and d-Au [17, 18].

Flow

As the created particles push each other away from the hot collision region, they acquire a flow velocity pointing towards the outside vacuum. Their momentum increases and the transverse momentum distribution is altered. Since this flow builds up throughout the evolution of the system, characterizing its properties may give information on both the partonic and the hadronic stages.

Anisotropic flow, appearing when the two nuclei do not collide head-on, has been extensively studied at RHIC [19, 20, 21]. Often, it is quantified by the Fourier coefficients in the expansion

$$\frac{d^2N}{dp_T d\phi} = \frac{dN}{dp_T}\left(1 + 2v_1 cos(\phi) + 2v_2 cos(2\phi) + 2v_4 cos(4\phi) + ...\right) \quad , \qquad (1.14)$$

displaying only the most contributing terms. Here, the ϕ angle is measured with respect to the reaction plane. The v_2 coefficient is often referred to as elliptic flow. In [22] it is argued that the data is consistent with a scenario where flow develops at both partonic and hadronic stages.

Strangeness Enhancement

The strangeness content in a QGP is believed to be enhanced from that of normal hadronic matter [23]. In a QGP there is a high concentration of u and d quarks. The quarks are fermions and the creation of $u\bar{u}$ and $d\bar{d}$ pairs might

be blocked due to the Pauli principle. Then the creation of $s\bar{s}$ pairs would be favored in spite of their larger mass.

An observed enhancement might however be explained in a purely hadronic scenario, where the abundance of strange quarks gradually grows in a chain of re-scattering processes. This complication can be solved by studying particles not likely to be produced by hadronic re-scattering, such as $\bar{\Lambda}$ (consisting of $\bar{u}\bar{d}\bar{s}$) and multi-strange baryons. The WA97 experiment at the CERN SPS concludes that there is an enhancement and that it actually increases with strangeness content [24].

J/Ψ Suppression

The J/Ψ particle is a bound state of a charm and an anti-charm quark ($c\bar{c}$). It is believed that the production of this resonance will be suppressed in a QGP [25], where the $c\bar{c}$ pair is separated due to *Debye screening* of the color charges. When the plasma hadronizes the separated quarks will likely combine with u and d quarks to open charm rather than J/Ψ.

The NA50 experiment at the CERN SPS has measured a decrease in the J/Ψ production rate in central Pb-Pb collisions [26]. Interpretations of J/Ψ suppression have to include the fact that it is possible also due to J/Ψ absorption in a dense hadronic medium. PHENIX has done a first measurement of J/Ψ production via decays to electron-positron pairs at midrapidity [27]. The statistics used in this analysis is however too low to make a conclusive statement about this signal. Results on high statistics measurements, both in the electron decay channel (at midrapidity) and in the muon decay channel (at forward and backward rapidities), are to be expected in the near future.

Properties of Light Vector Mesons

The light vector mesons ρ, ω and ϕ have been suggested as probes for a QGP, since their masses, widths and decay branching ratios may change in hot and dense matter. The ϕ meson with quark content $s\bar{s}$ is particularly interesting [28]. The main decay channel of this meson is $\phi \rightarrow K^+K^-$, and since the ϕ mass is only about 30 MeV above the mass of two kaons, the branching ratios are expected to change dramatically in a QGP, due to chiral symmetry restoration altering the quark masses.

A comparison between the decays of $\phi \rightarrow K^+K^-$ and $\phi \rightarrow e^+e^-$ requires very high statistics, since the branch to the latter is only about 0.03 % and the signal is hard to distinguish from the combinatorial background. PHENIX has presented first measurements of ϕ meson production [29]. With large statistical and systematic errors, the data show no significant change in the branching ratios.

Photon Production

Directly produced photons are of special interest [30]. Since they only interact electromagnetically, they have a mean free path much larger than the size of the reaction volume. Since there are no final state interactions, as with hadrons, the photons provide a direct probe of the initial stages of the collision. The direct photons are generally divided into *prompt photons* and *thermal photons*. The prompt photons are produced in initial hard parton scatterings, while thermal photons are produced in the possible QGP phase and the hadron gas phase. An increase in the emission of thermal photons is expected from a QGP.

The low production rate and huge background from hadronic decays, e.g. $\pi^0 \rightarrow \gamma\gamma$ and $\eta \rightarrow \gamma\gamma$, make the isolation of the prompt and thermal components delicate. PHENIX has presented first results on direct photon production [31]. At high p_T there are mostly prompt photons and the measurements indicate that they are not suppressed like the high p_T hadrons are. The results thus support the theory of a medium that quenches hard partons but leaves hard photons unaffected. Low p_T direct photons are not yet analyzed at RHIC.

Event-by-Event Fluctuations

Phase transitions are normally associated with large fluctuations. The QGP phase transition may yield anomalous fluctuations in e.g. particle multiplicities, ratios and transverse momenta. These fluctuations might be detectable in final state observables, some of which can be studied on an event-by-event basis [32]. The requirement of high statistics per event for such analyses is met at RHIC and LHC energies, where a high multiplicity of particles is produced.

The idea of event-by-event, *net-charge fluctuations* as a QGP signature is not directly related to the phase transition. The main issue is the distribution of electric charge in a QGP (where the quarks carry $\pm\,{}^1/_3$ or $\pm\,{}^2/_3$ unit charges), compared to the distribution in ordinary hadronic matter. It has been argued that the distribution of more evenly spread charge in a QGP would survive the phase transition back to hadronic matter [33, 34]. This signature will be discussed in detail in chapter 3.

Global Probes

As was seen in section 1.4 thermodynamic properties may in principle be extracted from measurable observables. Usually, the temperature T, entropy density s, and energy density ϵ are identified with measures closely related to the average transverse momentum $\langle p_T \rangle$, the hadron rapidity distribution dN/dy, and the transverse energy dE_T/dy, respectively [4]:

$$T \leftrightarrow \langle p_T \rangle \qquad\qquad s \leftrightarrow \frac{dN}{dy} \qquad\qquad \epsilon \leftrightarrow \frac{dE_T}{dy}$$

A first order QGP phase transition is revealed in a diagram of T as a function of ϵ. Such a figure would yield a rise, a plateau, and a second rise, due to the saturation of T during the mixed phase.

However, the measured momentum distribution of hadrons does not reflect the conditions at the early stages of the collision, and is often influenced by a collective flow of particles.

Chapter 2

The PHENIX Experiment

The Relativistic Heavy-Ion Collider, RHIC, at Brookhaven National Laboratory accelerates beams of nuclei, ranging from protons to gold. PHENIX [35] is one of four detectors operating to study collisions between the nuclei. The detector, built and operated by a collaboration of about 400 physicists and engineers, consists of various subsystems. The pad chambers constitute one of these. Construction and performance of these detectors is described in PAPER II.

2.1 Physics Goals

The primary goal of PHENIX is to detect the quark-gluon plasma and to characterize its properties. PHENIX offers the possibility to study many quantities related to the signatures described in section 1.6. The initial stages of the collisions can be characterized by measuring direct photons and lepton pairs. Detecting decays of mesons, such as J/Ψ and ϕ, may yield information on deconfinement and chiral symmetry restoration. Hadrons can be measured in a broad range of p_T and give information about freeze-out temperatures. Jet quenching is studied by detecting high-p_T jets from initial hard scattering processes. The collective motion of particles may be characterized from various flow analyses, and HBT correlation measurements can give information on source sizes. In addition, due to the large acceptance, different kinds of fluctuation measurements can be carried out.

Temperature and energy density of the system may be varied by changing beam energy and nuclear species. For instance, p-p and p-A collisions give information on purely hadronic effects, which may be a background for QGP signals.

A second goal of PHENIX is to study the spin structure of the nucleon. For this purpose RHIC accelerates beams of polarized protons.

2.2 Detector Subsystems

PHENIX consists of four spectrometer arms, trigger and vertex detectors and three magnets. The experimental layout is shown in figure 2.1. A brief description of the subsystems, arranged in three different categories, is given below.

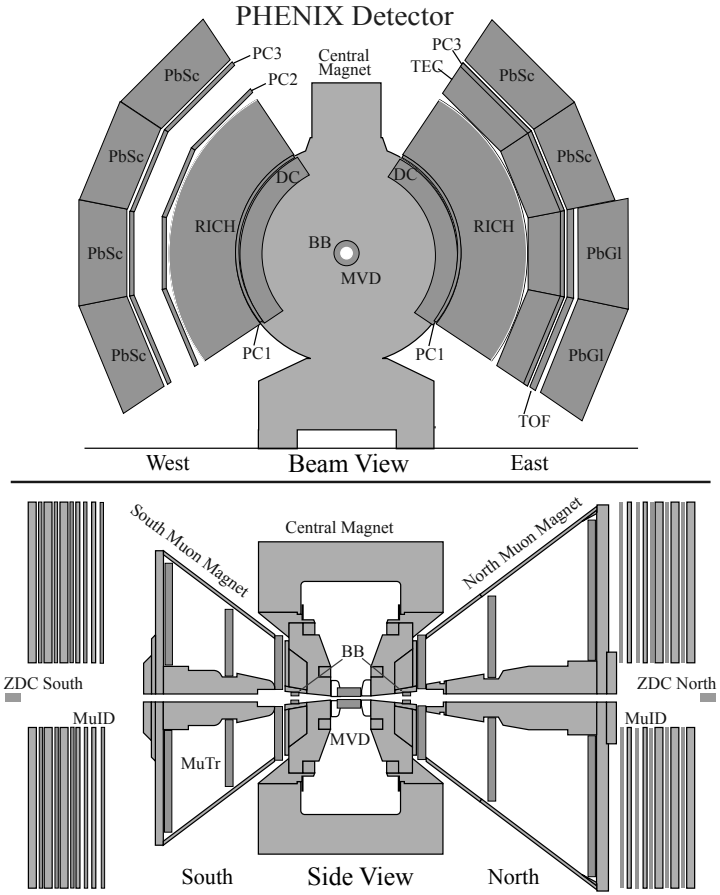

Figure 2.1: Experimental setup of the PHENIX detector system, as installed 2003, viewed along the beam axis (top) and from the side (bottom).

Vertex and Trigger Detectors

Two detector systems placed close to the beam axis are used for global event characterization.

The ***Beam-Beam Counters*** (BBC) consist of 64 Cerenkov detectors, arranged radially around the beam at 1.44 m from the center of the interaction region, with a pseudo-rapidity coverage of $3.0 < |\eta| < 3.9$. They provide the primary interaction trigger and measure the start time used for particle identification through time-of-flight measurements. Using the north-south time difference, they also provide a measure of the collision vertex position along the beam axis.

The ***Zero-Degree Calorimeters*** (ZDC) are situated 18 m upstream and downstream from the center of the interaction region. They measure the energy deposited by spectator neutrons from the collisions. Besides providing a trigger, they are used in combination with the BBCs for offline centrality selection.

Central Arm Spectrometers

The central arm spectrometers consist of tracking systems for charged particles and electromagnetic calorimetry. They cover ± 0.35 in pseudo-rapidity (η) and each arm spans 90° in azimuthal angle (ϕ). The magnetic field is supplied by the ***Central Magnet*** (CM) providing an axial field parallel to the beam.

The innermost tracking detectors are the ***Drift Chambers*** (DC), placed at a radial distance (r) of about 2 m from the origin. They are each composed of 40 planes of wires, arranged into 160 drift cells, providing precise tracking in the x-y plane and a high resolution p_T measurement from the charged particle trajectories.

There are three layers of ***Pad Chambers*** (PC1, PC2, PC3) on the west arm and two on the east arm (PC1,PC3). The Pad Chambers are pixel-based multi-wire proportional chambers that perform space point measurements of charged particles, enhancing the pattern recognition capabilities. 3-D tracking by the Pad Chambers minimize the influence of background from detector interactions and non-vertex decay particles and determine the polar angle (θ) of the trajectories. The Pad Chambers are described in more detail in section 2.5.

The ***Ring Imaging Cerenkov Counters*** (RICH) are the primary detectors for electron identification. They are composed of a gas vessel, thin reflection mirrors, and arrays of photo-multiplier tubes. Electron-pion discrimination is provided, since electrons above 18 MeV/c emit Cerenkov light in the gas radiator (CO_2), while pions below 4.9 GeV/c do not produce a signal.

The ***Time Expansion Chamber*** (TEC), placed on the east arm only, contains four planes of wires. Like the DC, the TEC provides tracking in the r-ϕ plane. It also contributes to electron-pion discrimination via dE/dx measurements, and provides additional high momentum resolution for high-p_T

particles. From RHIC run period 3 it also operates as a transition radiation detector for electron identification.

The ***Time-Of-Flight Detector*** (TOF), located on the east arm only, serves as the primary particle identification device for charged hadrons. It contains plastic scintillation counters with photo-multiplier tubes, and provides high-resolution flight-time measurements.

The ***Electromagnetic Calorimeters*** (EMC) provide photon identification, particle energy and time-of-flight measurements. 25% of the EMC are lead-glass calorimeters (PbGl) providing good energy resolution. The rest is made up of lead-scintillator calorimeters providing fairly good timing resolution.

Muon Spectrometers

The two forward spectrometers use radial magnetic fields. Each contain a ***Muon Tracker*** (MuTr) followed by a ***Muon Identifier*** (MuID), both with full azimuthal coverage. The Muon Trackers consist of multi-plane cathode strip chambers for tracking. The muon identifiers are composed of alternating layers of steel absorbers and low resolution tracking layers of streamer tubes. This combination provides a discrimination of pions, since they are stopped in the steel absorbers.

2.3 Data Acquisition

Signals from the various subsystems are processed by *Front End Electronics* (FEE) placed close to the detectors. The FEEs convert these signals into digital "event fragments". Governed by the RHIC clock, which is synchronized with the beam crossings at 9.4 MHz, the FEEs of the trigger system send output to the *level-1 trigger* (LVL1). When the trigger accepts an event, data from the various subsystems are delivered via fiber-optic cable to the *Data Collection Modules* (DCM). The DCMs perform zero suppression, error checking and data reformatting. The data are then assembled into complete events in the *Event Builder* (EvB) that also provides an environment for the *level-2 trigger* (LVL2) to operate, in order to further enrich the sample of accepted events. Finally, the data are recorded to disk for storage.

During the 2004 Au+Au run, the event rate routinely achieved by the data acquisition system was about 2 kHz.

2.4 Event Reconstruction

The raw data are processed offline to produce data summaries of the events, which are later used in various physics analyses. When reconstructing particle

tracks in the central arms (see PAPER I), a track model primarily based on DC and PC1 information is utilized. Trajectories and momenta are reconstructed using a field-integral map to account for the non-uniform magnetic field. Figure 2.2 shows Drift Chamber hits that are used to reconstruct a track. The

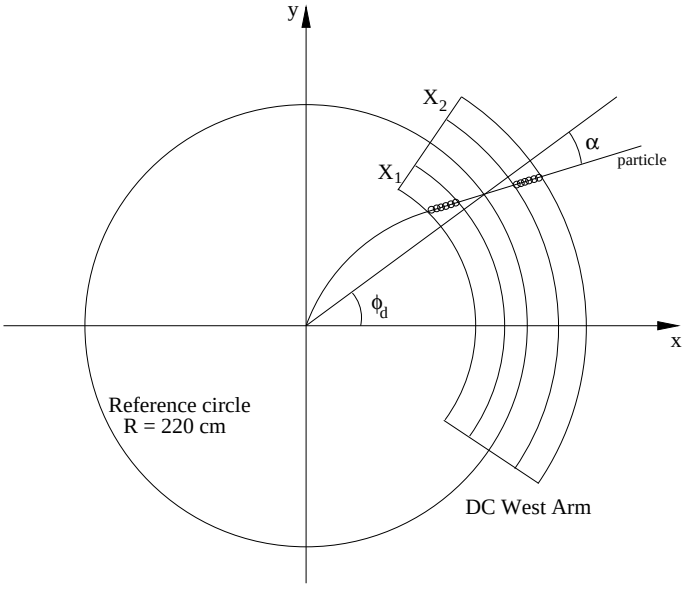

Figure 2.2: A charged track passing through one of the Drift Chambers. The open circles show the detector hits. (X_1 and X_2 are two sets of wire planes inside the DC.)

sign of the inclination angle α determines the charge of the particle, while the absolute value gives the transverse momentum. Information on the longitudinal momentum is derived from the PC1 z coordinate. When the trajectory is determined, its projected intersections with various detectors are recorded in order to facilitate inter-detector hit association.

Simulated events are reconstructed using the same software code with minor modifications. The simulated data files are produced using an event generator, such as RQMD [36] or Hijing [37]. The output from the event generator is fed into a simulation package for PHENIX, called PISA (PHENIX Integrated Simulation Application), which is based on GEANT [38]. Specific code has been developed to simulate the response for each detector.

2.5 The Pad Chambers

As was mentioned in section 2.2 the Pad Chambers are pixel-based multi-wire proportional chambers, used in the central arm tracking system. The three layers, PC1, PC2 and PC3, are placed at roughly 2.5 m, 4.2 m and 5 m radial distance from the beam. (There is no PC2 in the east arm.) They cover about 0.7 units in pseudo-rapidity ($|\eta| < 0.35$) and 90° in azimuth in each arm, i.e. the full aperture of the spectrometer arms.

2.5.1 The Pixel Pattern

The Pad Chamber readout is based on the induced charge on the cathode planes, which are segmented into readout pads. To reduce the number of readout channels, the pads consist of 9 copper rectangles called pixels, arranged in an interleaved pattern, as illustrated in figure 2.3. A cell consists of one center

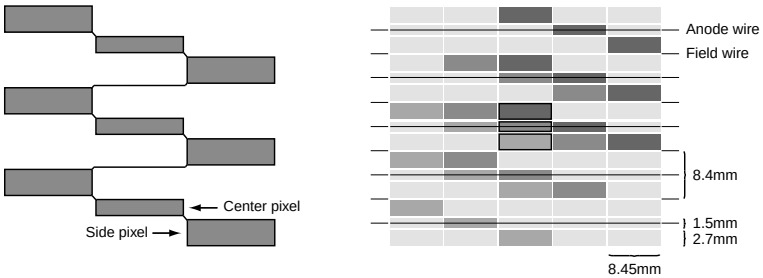

Figure 2.3: A pad consists of 9 pixels (left). The pixel layout showing three fired pads combined to form one fired cell (right). The sizes of the center and side pixels are chosen so that they collect an equal amount of charge. The center pixel is closer to the avalanche and therefore designed somewhat smaller. (Values are for PC1.)

pixel and two side pixels belonging to adjacent pads. A valid hit is formed when all three pads corresponding to these pixels fire, i.e. when the collected charge of each pad is above a set threshold. A set of adjoining fired cells is called a cluster.

2.5.2 Cluster Reconstruction

The main steps in the pad chamber reconstruction algorithm are shown in figure 2.4. The software code is fed with a list of fired pads, either from simulated events or from data. In the first case there is a response simulator that processes PISA hit information. For all tracks, the deposition of charge on the

chamber wires is sampled from a Landau distribution with an addition of random electronics noise. The pads that receive charge above a certain threshold value are passed on for reconstruction.

The first step in the algorithm is to combine the information from the list of pads to find all fired cells. The implementation of this step was recently changed, reducing the processing time by a factor of two or more (depending on the multiplicity of events). The improvement lies in omitting the very time consuming method of checking *all* cells, for information about their pads. Instead, only the cells with fired pads are checked. In the second step, the produced list of cells is processed to form clusters of adjacent cells. Finally, the coordinates of these clusters are determined and passed on to be used in the charged particle tracking.

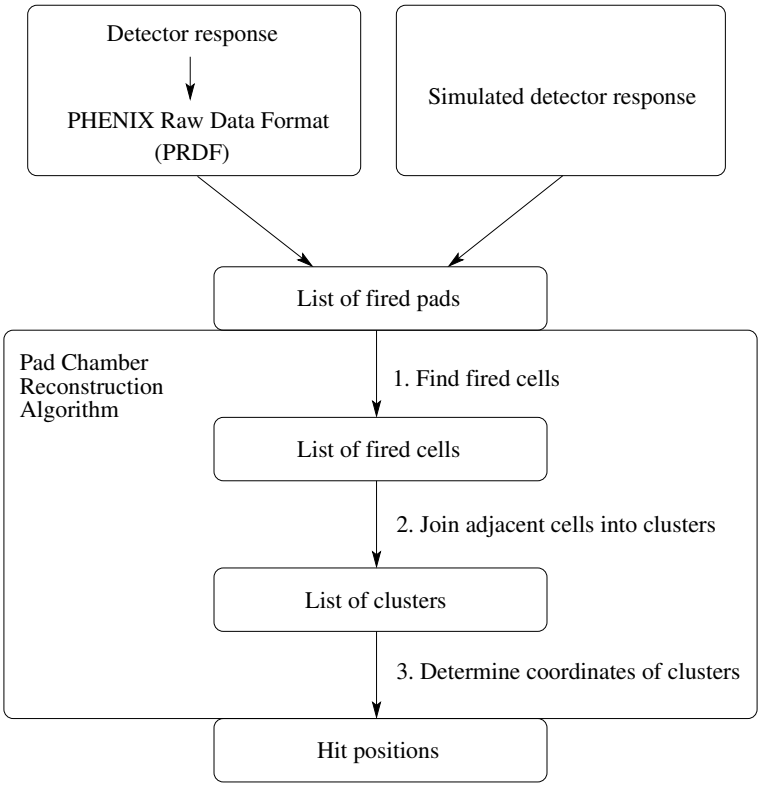

Figure 2.4: Flow diagram of the pad chamber reconstruction code.

2.5.3 Online Monitoring and Calibration

The performance of all PHENIX detector systems are carefully monitored during data taking. The so-called online monitoring software developed for the pad chambers displays wire activity and cluster size distributions for all high-voltage sectors, making it possible to instantly detect high-voltage trips and changes in efficiency.

A large effort has also been put into developing software to automatically calibrate the detectors. For the pad chamber subsystem this so-called online calibration is performed as a search for inactive and "hot" TGLD chips. Each pad chamber readout card (ROC) has three TGLD chips, each connected to 16 pads. Figure 2.5 shows the number of fired pads per event for all TGLDs. (There are totally 10,800.) The data are taken from a 200 GeV Au+Au run.

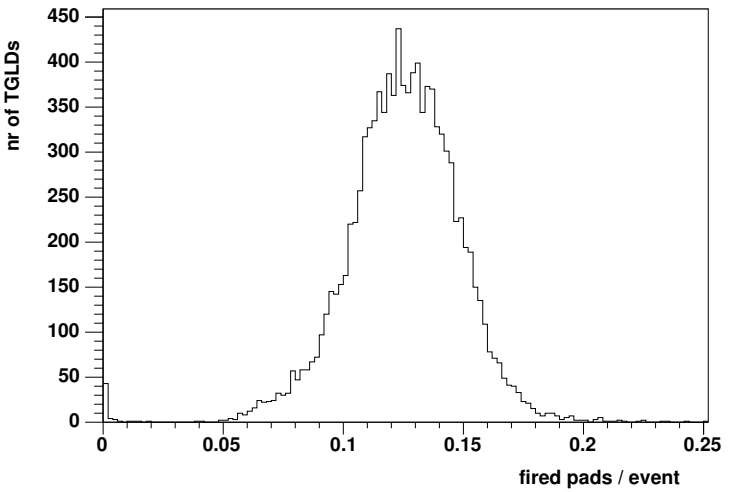

Figure 2.5: Histogram of fired pads per event, filled once for each TGLD. The data are from a 200 GeV Au+Au run.

With statistics of a couple of thousand events, the totally or partly inactive TGLDs are clearly separated from the others. For p+p and d+Au the occupancy decreases and the method requires higher event statistics (about a factor of 10) and the lower limit has to be set close to zero. Actually, the same limit of 0.0001 has been used for all colliding species. The "hot" TGLDs (not shown in the figure) are also clearly separated having 16 pads fired per event.

Before submitting the information about malfunctioning TGLDs to the database, a quality and assurance test is made on the data. All high voltage sectors are checked to make sure that the number of clusters per event and

wire is above a certain threshold value.

The number of malfunctioning ROCs amounts to about three percent after three years of running, and increases very slowly with time. A large part of the problematic ROCs are located in the PC3 east chambers.

2.5.4 Efficiency and Position Resolution

Before installation, each Pad Chamber was tested with cosmic rays. In studies of efficiency and position resolution, a triggering system with large plastic scintillators read out by photomultipliers were used. A more detailed description of the setup and measurements can be found in PAPER II.

The efficiency measurements were carried out by varying both the anode wire voltage and the pad threshold setting. The results are shown in figure 2.6. The operating voltages are set to 1700 V for PC1, 1840 V for PC2, and

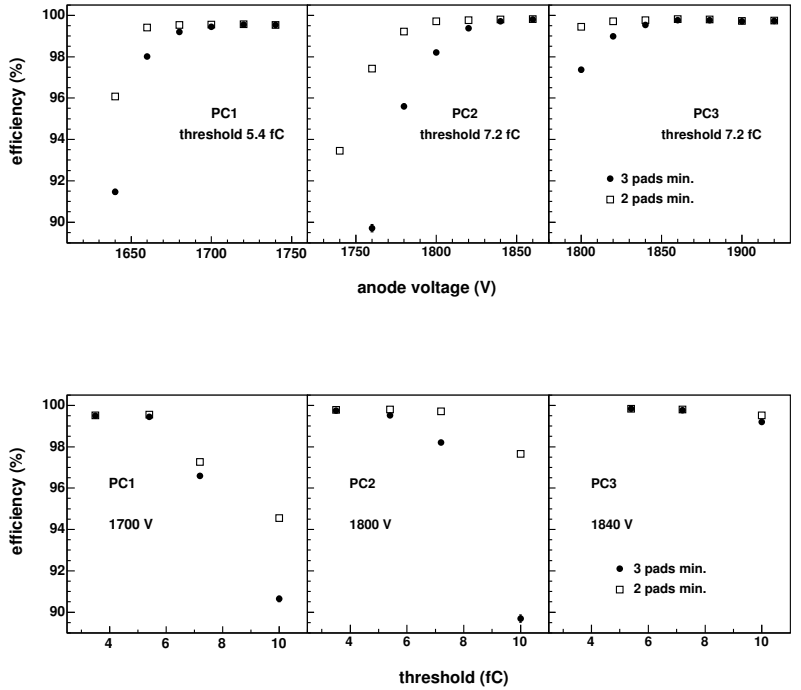

Figure 2.6: Efficiency curves for PC1/2/3 with

- *varying high voltage and constant threshold (top)*
- *varying threshold and constant high voltage (bottom)*

The results are shown also for the case when only two fired pads in a cell are required for a valid hit (2 pads min.).

1880 V for PC3. The operating thresholds are set to 5.4 fC, 7.2 fC, and 7.2 fC respectively. Efficiency values for these settings are shown in table 2.1.

	PC1	*PC2*	*PC3*
Efficiency	99.6 %	99.8 %	99.8 %

Table 2.1: Efficiency at operational settings.

In the position resolution measurements, performed for PC1 and PC2, an additional chamber (PC1) was used as a reference. The results are presented in table 2.2.

Position resolution (σ)	*PC1*	*PC2*
Along wires	1.7 mm	3.1 mm
Across wires	3.4 mm	5.0 mm

Table 2.2: Position resolution along and across wires.

Chapter 3

Net-Charge Fluctuations

Event-by-event fluctuations of the net charge in local regions of phase space have been proposed as a probe of the QGP state [33, 34]. In section 3.1 the physics motivation behind this idea is presented, along with some derivations and predictions. Simulations of some factors influencing the magnitude of the fluctuations are described in PAPER IV. In section 3.2 the analyses of PHENIX data from the two first run periods of Au+Au data taking are presented.

3.1 Theoretical Approach

3.1.1 Physics Motivation

Consider a scenario where a source emits particles with electric charge +1 and -1 with probabilities p_+ and p_-. In each event, a fixed number of charged particles $n_{ch} = n_+ + n_-$ is emitted. The magnitude of the event-by-event fluctuations in net charge $Q = n_+ - n_-$ can be calculated from the variance $\mathrm{V}(Q)$.

$$\begin{aligned} \mathrm{V}(Q) &\equiv \langle Q^2 \rangle - \langle Q \rangle^2 = \\ &= \langle n_+^2 \rangle + \langle n_-^2 \rangle - 2\langle n_+ n_- \rangle - \langle n_+ \rangle^2 - \langle n_- \rangle^2 + 2\langle n_+ \rangle \langle n_- \rangle = \\ &= \mathrm{V}(n_+) + \mathrm{V}(n_-) - 2\mathrm{cov}(n_+, n_-) = \\ &= 4p_+p_- \cdot n_{ch} \end{aligned} \tag{3.1}$$

since, in this case, $\mathrm{V}(n_+) = \mathrm{V}(n_-) = p_+p_-n_{ch} = -\mathrm{cov}(n_+, n_-)$.

Different measures have been suggested for the study of net-charge fluctuations. Since the variance of Q scales with n_{ch}, one of the most straightforward choices is the normalized variance $v(Q)$, defined in the following way:

$$v(Q) \equiv \frac{\mathrm{V}(Q)}{\langle n_{ch} \rangle} \tag{3.2}$$

Here the mean value of n_{ch} is used, giving the possibility to study data samples containing events with varying n_{ch}.

Now consider the two scenarios of heavy-ion collisions illustrated in figure 1.4. The purely hadronic scenario would very much resemble the example above, with the main charge carriers being pions. With $p_+ = p_- = {}^1/_2$ in (3.1) the normalized variance is simply $v(Q) = 1$.

In a QGP, assuming thermal distributions ($\mathrm{V}(n_{ch}) = \langle n_{ch} \rangle$) and no correlations, taking only u and d quarks into account,

$$\mathrm{V}(Q) \equiv \langle Q^2 \rangle - \langle Q \rangle^2 = q_u^2 \langle n_{u+\bar{u}} \rangle + q_d^2 \langle n_{d+\bar{d}} \rangle \tag{3.3}$$

If the quark flavors appear with equal probability, the normalized variance is

$$v(Q) = \frac{1}{2}(q_u^2 + q_d^2) = \frac{1}{2}\left(\frac{4}{9} + \frac{1}{9}\right) = \frac{5}{18} \tag{3.4}$$

This value is however not directly measurable in experiments. The essential question is whether the distribution of more evenly spread charge in a QGP survives the hadronization process, in order to be observed as a reduction in fluctuation.

Jeon and Koch have made a simple thermal model calculation to predict the magnitude of the fluctuations after hadronization [33]. They state a relationship between the number of created pions and the number of quarks and gluons inside the plasma:

$$\langle n_\pi \rangle = \langle n_g \rangle + \frac{4.2}{3.6}[\langle n_{u+\bar{u}} \rangle + \langle n_{d+\bar{d}} \rangle] \tag{3.5}$$

Using this result in (3.3), assuming that ${}^2/_3$ of the pions are charged, and that $\langle n_{u+\bar{u}} \rangle = \langle n_{d+\bar{d}} \rangle = \frac{1}{2}\langle n_g \rangle$,

$$v(Q) = \frac{\frac{4}{9} + \frac{1}{9}}{\frac{2}{3}\left(2 + 2 \cdot \frac{4.2}{3.6}\right)} = \frac{5}{26} \approx 0.19 \tag{3.6}$$

A lattice calculation result of $v(Q) = 0.25$ is also presented in [33], and it is argued that these reduced fluctuations should be possible to observe in experiments.

3.1.2 Influences on the Fluctuations

When performing net-charge fluctuation measurements, one has to be aware that there are a few – more or less trivial – effects changing the magnitude of the net-charge fluctuations.

Global Charge Conservation and Charge Asymmetry

Since charge is a globally conserved quantity, the fluctuation measurements are strongly dependent on the acceptance of the detector. If all charged particles, denoted N_{ch}, are detected in each event, i.e. with 100% detection efficiency and a 4π detector, there are no fluctuations, and $v(Q) = 0$.

Another property that may alter the magnitude of the fluctuations is charge asymmetry, i.e. when – for some reason – more positive than negative particles are detected or vice versa. This can be seen in equation (3.1). With $\varepsilon \equiv p_+ - p_-$ representing a small excess of positive particles, $v(Q) = 4p_+p_- = 1 - \varepsilon^2$ in this case.

Global charge conservation and charge asymmetry can be incorporated into a derivation of a more general result for $v(Q)$. Let p_a denote the fraction of observed charged particles among all charged particles in the event. In the following derivation both n_{ch} and $n_+(n_-)$ are binomially distributed (with $n_{ch} \in \mathrm{Bin}(p_a, N_{ch})$ and $n_\pm \in \mathrm{Bin}(p_a, p_\pm N_{ch})$), and the probability distribution for N_{ch} is denoted Π. It is also assumed that the ratio between N_+ and N_- is constant [1]. First, a few building blocks needed to find the expression for $\mathrm{V}(Q)$:

$$\langle n_+ \rangle = \sum_{N_{ch}} \Pi p_a p_+ N_{ch} = p_a p_+ \langle N_{ch} \rangle \tag{3.7}$$

$$\langle n_- \rangle = \sum_{N_{ch}} \Pi p_a p_- N_{ch} = p_a p_- \langle N_{ch} \rangle \tag{3.8}$$

$$\begin{aligned} \langle n_+^2 \rangle &= \sum_{N_{ch}} \Pi \left[p_a(1-p_a)p_+ N_{ch} + p_a^2 p_+^2 N_{ch}^2 \right] = \\ &= p_a(1-p_a)p_+ \langle N_{ch} \rangle + p_a^2 p_+^2 \langle N_{ch}^2 \rangle \end{aligned} \tag{3.9}$$

[1] Global charge conservation would normally imply that $N_+ - N_-$ is constant and equal to the number of protons in the colliding nuclei. However, the particles observed in the central region of phase space reflect the participant parts of the nuclei rather than the whole nuclei. It is thus reasonable to expect that $N_+ - N_-$ is proportional to N_{ch}, which is also supported by the experimental data (see figure 3.13 on page 43).

$$\langle n_-^2 \rangle = \sum_{N_{ch}} \Pi \left[p_a(1-p_a) p_- N_{ch} + p_a^2 p_-^2 N_{ch}^2 \right] =$$

$$= p_a(1-p_a) p_- \langle N_{ch} \rangle + p_a^2 p_-^2 \langle N_{ch}^2 \rangle \tag{3.10}$$

$$\langle n_+ n_- \rangle = \sum_{N_{ch}} \Pi p_a^2 p_+ p_- N_{ch}^2 = p_a^2 p_+ p_- \langle N_{ch}^2 \rangle \tag{3.11}$$

Using equations (3.7) - (3.11) the expression for V(Q) is

$$\begin{aligned}
\mathrm{V}(Q) &\equiv \langle Q^2 \rangle - \langle Q \rangle^2 = \langle (n_+ - n_-)^2 \rangle - \langle n_+ - n_- \rangle^2 = \\
&= \langle n_+^2 \rangle + \langle n_-^2 \rangle - 2\langle n_+ n_- \rangle - \langle n_+ \rangle^2 - \langle n_- \rangle^2 + 2\langle n_+ \rangle \langle n_- \rangle = \\
&= p_a(1-p_a) p_+ \langle N_{ch} \rangle + p_a^2 p_+^2 \langle N_{ch}^2 \rangle + p_a(1-p_a) p_- \langle N_{ch} \rangle \\
&\quad + p_a^2 p_-^2 \langle N_{ch}^2 \rangle - 2 p_a^2 p_+ p_- \langle N_{ch}^2 \rangle - p_a^2 p_+^2 \langle N_{ch} \rangle^2 - p_a^2 p_-^2 \langle N_{ch} \rangle^2 \\
&\quad + 2 p_a^2 p_+ p_- \langle N_{ch} \rangle^2 = \\
&= p_a(1-p_a) \langle N_{ch} \rangle + p_a^2 (p_+^2 + p_-^2 - 2 p_+ p_-) \langle N_{ch}^2 \rangle - \\
&\quad - p_a^2 (p_+^2 + p_-^2 - 2 p_+ p_-) \langle N_{ch} \rangle^2 = \\
&= (1-p_a) \langle n_{ch} \rangle + p_a^2 \varepsilon^2 \mathrm{V}(N_{ch})
\end{aligned} \tag{3.12}$$

V(n_{ch}) can be used in order to express V(N_{ch}) in terms of n_{ch}:

$$\begin{aligned}
\mathrm{V}(n_{ch}) &\equiv \langle n_{ch}^2 \rangle - \langle n_{ch} \rangle^2 = \\
&= \sum_{N_{ch}} \Pi \left[p_a(1-p_a) N_{ch} + p_a^2 N_{ch}^2 \right] - p_a^2 \langle N_{ch} \rangle^2 = \\
&= p_a(1-p_a) \langle N_{ch} \rangle + p_a^2 \langle N_{ch}^2 \rangle - p_a^2 \langle N_{ch} \rangle^2 = \\
&= p_a(1-p_a) \langle N_{ch} \rangle + p_a^2 \mathrm{V}(N_{ch})
\end{aligned} \tag{3.13}$$

Using (3.13) in (3.12) yields

$$\begin{aligned} \mathrm{V}(Q) &= (1-p_a)\langle n_{ch}\rangle + \varepsilon^2 \cdot (\mathrm{V}(n_{ch}) - (1-p_a)\langle n_{ch}\rangle) = \\ &= (1-p_a)(1-\varepsilon^2)\langle n_{ch}\rangle + \varepsilon^2 \mathrm{V}(n_{ch}) \end{aligned} \tag{3.14}$$

and the result can finally be given with normalized variances:

$$v(Q) = (1-p_a)(1-\varepsilon^2) + \varepsilon^2 v(n_{ch}) \tag{3.15}$$

Background and Detector Efficiency

Experimental effects, such as background contributions and detection inefficiencies, also influence the magnitude of the fluctuations. The effect of a background can be estimated realizing that the observed variance $\mathrm{V}_{obs}(Q)$ is the sum of the true and background contributions.

$$\mathrm{V}_{obs}(Q) = \mathrm{V}_{true}(Q) + \mathrm{V}_{bkg}(Q) \tag{3.16}$$

With f_{bkg} being the fraction of the particles coming from background,

$$\begin{aligned} v_{obs}(Q) &= (1-f_{bkg}) \cdot v_{true}(Q) + f_{bkg} \cdot v_{bkg}(Q) = \\ &= 1 - (1-f_{bkg})(1-v_{true}(Q)) - f_{bkg}(1-v_{bkg}(Q)) \end{aligned} \tag{3.17}$$

If the background consists of uncorrelated positive and negative particles, this equation is reduced to

$$v_{obs}(Q) = 1 - (1-f_{bkg})(1-v_{true}(Q)) \quad , \tag{3.18}$$

i.e. random background contributions move a reduced $v(Q)$ towards the value 1, the stochastic scenario. Detection inefficiencies affect the fluctuations in a similar way. Assuming that the detection efficiency p_e is equal for positive and negative particles,

$$v_{obs}(Q) = 1 - p_e(1-v_{true}(Q)) \tag{3.19}$$

A combined result with an uncorrelated background can be obtained by substituting $v_{obs}(Q)$ of (3.19) into $v_{true}(Q)$ in (3.18):

$$v_{obs}(Q) = 1 - p_e(1-f_{bkg})(1-v_{true}(Q)) \tag{3.20}$$

Neutral Resonance Decays

Neutral resonances, such as ρ and ω, introduce positive correlations between n_+ and n_- and therefore reduce the fluctuations. In [33] Jeon and Koch estimate the reduction to $v(Q) = 0.75$. This effect is examined in simulations in PAPER IV.

3.1.3 Some Comparisons Between Various Measures

As was mentioned earlier, several measures, along with $v(Q)$, have been suggested for characterizing the fluctuations. Here are the definitions of some of them. (The definition of $v(Q)$ is given once more for direct comparison.)

$$v(Q) \equiv \frac{\mathrm{V}(Q)}{\langle n_{ch}\rangle} = \frac{1}{\langle n_{ch}\rangle}\left\langle (Q-\langle Q\rangle)^2\right\rangle \tag{3.21}$$

$$v(R) \equiv \langle n_{ch}\rangle\cdot \mathrm{V}(R) = \langle n_{ch}\rangle\left\langle \left(\frac{n_+}{n_-}-\left\langle\frac{n_+}{n_-}\right\rangle\right)^2\right\rangle \quad [33] \tag{3.22}$$

$$\Gamma \equiv \frac{1}{\langle n_{ch}\rangle}\left\langle\left(Q-\frac{\langle Q\rangle}{\langle n_{ch}\rangle}n_{ch}\right)^2\right\rangle \quad [39] \tag{3.23}$$

$$\nu_{dyn} \equiv \left\langle\left(\frac{n_+}{\langle n_+\rangle}-\frac{n_-}{\langle n_-\rangle}\right)^2\right\rangle - \left(\frac{1}{\langle n_+\rangle}+\frac{1}{\langle n_-\rangle}\right) \quad [40] \tag{3.24}$$

In the stochastic scenario it was shown that $v(Q)=1-\varepsilon^2$, independent of n_{ch}. However, $v(R)$ as a function of n_{ch} suffers from a skewness. In the case where $\varepsilon=0$, $v(R)$ approaches the value 4 as n_{ch} increases. For fixed n_{ch} with $\varepsilon\neq 0$

$$\mathrm{V}(R)=\mathrm{V}\left(\frac{n_+}{n_-}\right)=\mathrm{V}\left(\frac{n_+}{n_{ch}-n_+}\right)=\mathrm{V}\left(\frac{n_{ch}}{n_{ch}-n_+}-1\right)=$$

$$=\mathrm{V}\left(\frac{n_{ch}}{n_-}\right)=n_{ch}^2\cdot\mathrm{V}\left(\frac{1}{n_-}\right)\approx n_{ch}^2\cdot\frac{1}{\langle n_-\rangle^4}\cdot\mathrm{V}(n_-)=$$

$$=n_{ch}^2\cdot\frac{1}{(p_-n_{ch})^4}\cdot p_+p_-n_{ch}=\frac{1}{n_{ch}}\frac{\frac{1-\varepsilon^2}{4}}{\frac{(1-\varepsilon)^4}{16}}=\frac{4}{n_{ch}}\frac{1+\varepsilon}{(1-\varepsilon)^3}=$$

$$=\frac{4}{n_{ch}}[1+4\varepsilon+O(\varepsilon^2)] \tag{3.25}$$

and consequently

$$v(R)=4+16\varepsilon+O(\varepsilon^2) \tag{3.26}$$

which shows that $v(R)$ is more sensitive than $v(Q)$ to an asymmetry in charge.

The Γ measure is quite similar to $v(Q)$. Since $\frac{\langle Q\rangle}{\langle n_{ch}\rangle} = \varepsilon$ and $\langle Q - \varepsilon \cdot n_{ch}\rangle = 0$, equation (3.23) can be rewritten to yield

$$\Gamma = \frac{1}{\langle n_{ch}\rangle}\mathrm{V}(Q - \varepsilon \cdot n_{ch}) =$$

$$= \frac{1}{\langle n_{ch}\rangle}\left[\langle Q^2\rangle + \varepsilon^2\langle n_{ch}^2\rangle - 2\varepsilon\langle Q \cdot n_{ch}\rangle - \langle Q\rangle^2 - \varepsilon^2\langle n_{ch}\rangle^2 + 2\varepsilon\langle Q\rangle\langle n_{ch}\rangle\right] =$$

$$= \frac{1}{\langle n_{ch}\rangle}\left[\mathrm{V}(Q) + \varepsilon^2\mathrm{V}(n_{ch}) - 2\varepsilon^2\mathrm{V}(n_{ch})\right] = \frac{1}{\langle n_{ch}\rangle}\left[\mathrm{V}(Q) - \varepsilon^2\mathrm{V}(n_{ch})\right] =$$

$$= v(Q) - \varepsilon^2 v(n_{ch}) \tag{3.27}$$

where the relation below was used.

$$\langle Q \cdot n_{ch}\rangle = \sum_{n_{ch}} \Pi_{n_{ch}} \sum_{n_+} \Pi_{n_+}(2n_+ - n_{ch})n_{ch} =$$

$$= 2\sum_{n_{ch}} \Pi_{n_{ch}} n_{ch} \sum_{n_+} \Pi_{n_+} n_+ - \sum_{n_{ch}} \Pi_{nch} n_{ch}^2 =$$

$$= (2p_+ - 1)\langle n_{ch}^2\rangle =$$

$$= \varepsilon\langle n_{ch}^2\rangle \tag{3.28}$$

If $\varepsilon = 0$, (3.27) shows that Γ is equal to $v(Q)$. Comparing with (3.15) it is seen that when using Γ the $v(n_{ch})$ dependence is gone. The corresponding result for Γ is

$$\Gamma = (1 - p_a)(1 - \varepsilon^2) \tag{3.29}$$

The ν_{dyn} measure, equation (3.24), can also be written

$$\nu_{dyn} = \left\langle \left(\frac{n_+}{\langle n_+ \rangle} - \frac{n_-}{\langle n_- \rangle} \right)^2 \right\rangle - \left(\frac{1}{\langle n_+ \rangle} + \frac{1}{\langle n_- \rangle} \right) =$$

$$= \frac{4}{\langle n_{ch} \rangle^2} \left\langle \left(\frac{n_+}{1+\varepsilon} - \frac{n_-}{1-\varepsilon} \right)^2 \right\rangle - \frac{2}{\langle n_{ch} \rangle} \left(\frac{1}{1+\varepsilon} + \frac{1}{1-\varepsilon} \right) =$$

$$= \frac{4}{\langle n_{ch} \rangle} \left[\frac{\left\langle \left(\frac{n_+}{1+\varepsilon} - \frac{n_-}{1-\varepsilon} \right)^2 \right\rangle}{\langle n_{ch} \rangle} - \frac{1}{1-\varepsilon^2} \right] \tag{3.30}$$

and with charge symmetry, $\varepsilon = 0$,

$$\nu_{dyn} = \frac{4}{\langle n_{ch} \rangle} \left[v(Q) - 1 \right] \tag{3.31}$$

It can easily be shown that, in the stochastic scenario, $\nu_{dyn} = 0$ and the result for ν_{dyn} corresponding to equations (3.15) and (3.29) is

$$\nu_{dyn} = -\frac{4}{\langle n_{ch} \rangle} \cdot \frac{p_a}{1-\varepsilon^2} \tag{3.32}$$

For a given set of events this would yield a constant value, since $\langle n_{ch} \rangle = p_a \langle N_{ch} \rangle$. This value would be unaffected by an efficiency less than 100% [40], but would change when background contributions are added, as can be seen in PAPER IV.

Some features and differences between the measures defined in equations (3.21) - (3.24) are also addressed in various scenarios described in PAPER IV. Using a Monte Carlo technique, effects of global charge conservation, charge asymmetry, neutral resonance decays, experimental inefficiencies and background are studied. At the end, a simplified model of hadronization from a QGP is also tested.

3.2 Analysis of PHENIX Au+Au Data

3.2.1 $\sqrt{s_{NN}}$ =130 GeV

During the first run period RHIC provided Au-Au collisions at $\sqrt{s_{NN}} = 130$ GeV. The primary interaction trigger was based on information from the two BBCs. The trigger required a coincidence where at least two photo-multipliers on each side fired. From simulations this was found to correspond to 92% of the nuclear interaction cross section of 7.2 barns. A total of about half a million such minimum bias events were used in the net-charge fluctuation analysis, which is based on information from the drift chamber and the first pad chamber plane in the west tracking arm. These detectors cover approximately 0.7 units in pseudo-rapidity and 90° in azimuth. The PC3 west chambers were not yet installed during this first physics run period. The vertex positions of the collisions were retrieved from the time difference between the two BBCs. A rather tight vertex cut of $|z| < 17$ cm was applied to get a homogeneous event sample, where background from secondary interactions in the magnet iron was minimized.

Simulations Using RQMD

Results from the data were compared to simulations using the RQMD [36] event generator, PISA and detector response code. The simulations also gave information on reconstruction efficiencies and background contributions. The reconstruction efficiency was shown to fall rapidly for particles with p_T below 0.2 GeV/c, implying exclusion of tracks with $p_T < 0.2$ GeV/c from the real data sample. The overall efficiency for detecting charged particles was then found to be about 80%, both for positive and negative particles. This figure includes inactive detector parts, e.g. inactive pad chamber ROCs. Background contributions, e.g. from interactions in detector material and weak decays, were estimated to about 20% of the reconstructed tracks.

The acceptance coverage p_a of the detectors was estimated from the simulations to be 0.018. A value of $\varepsilon = 0.078$ was measured from the data sample. The expected reduction in the net-charge fluctuations, due to global charge conservation, then yields (assuming the background is uncorrelated)

$$\begin{aligned} v(Q) &= 1 - p_e \cdot (1 - f_{bkg}) \left[1 - (1 - p_a)(1 - \varepsilon^2)\right] \quad = \\ &= 1 - 0.8 \cdot (1 - 0.2) \left[1 - (1 - 0.018)(1 - 0.078^2)\right] \quad \approx \\ &\approx 0.985 \end{aligned} \tag{3.33}$$

Results

Figure 3.1 shows $4 \cdot v(Q)$ and $v(R)$ for each value of n_{ch}. The data points are

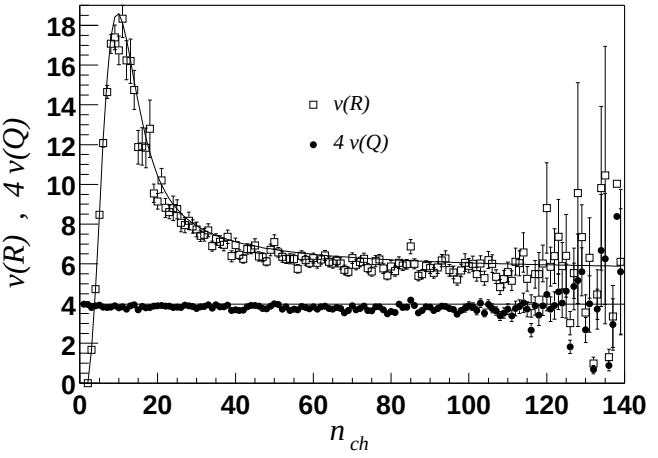

Figure 3.1: $4 \cdot v(Q)$ and $v(R)$ for fixed values of n_{ch}. Solid curves show the stochastic behavior, calculated using equations (3.34) - (3.37).

compared to a purely stochastic behavior (solid curves), calculated from

$$\langle Q \rangle = \sum_{i=0}^{n_{ch}} (2i - n_{ch}) \left(\begin{array}{c} n_{ch} \\ i \end{array} \right) p_+^{n_{ch}-i} \cdot p_-^i \tag{3.34}$$

$$\langle Q^2 \rangle = \sum_{i=0}^{n_{ch}} (2i - n_{ch})^2 \left(\begin{array}{c} n_{ch} \\ i \end{array} \right) p_+^{n_{ch}-i} \cdot p_-^i \tag{3.35}$$

$$\langle R \rangle = \frac{1}{A} \sum_{i=1}^{n_{ch}-1} \frac{n_{ch} - i}{i} \left(\begin{array}{c} n_{ch} \\ i \end{array} \right) p_+^{n_{ch}-i} \cdot p_-^i \tag{3.36}$$

$$\langle R^2 \rangle = \frac{1}{A} \sum_{i=1}^{n_{ch}-1} \left(\frac{n_{ch} - i}{i} \right)^2 \left(\begin{array}{c} n_{ch} \\ i \end{array} \right) p_+^{n_{ch}-i} \cdot p_-^i \tag{3.37}$$

where $A = 1 - p_+^{n_{ch}} - p_-^{n_{ch}}$ is the new normalization needed when discarding events with n_+ or n_- equal to zero, in the case of R. The figure shows that

the use of $v(R)$ introduces complications. $v(R)$ has a strong dependence on n_{ch} and ε. The values are understood only when comparing to the stochastic curve, but for event classes with varying n_{ch} it is not straightforward to calculate such a curve.

Figure 3.2 displays $v(Q)$ as a function of increasing centrality. The cen-

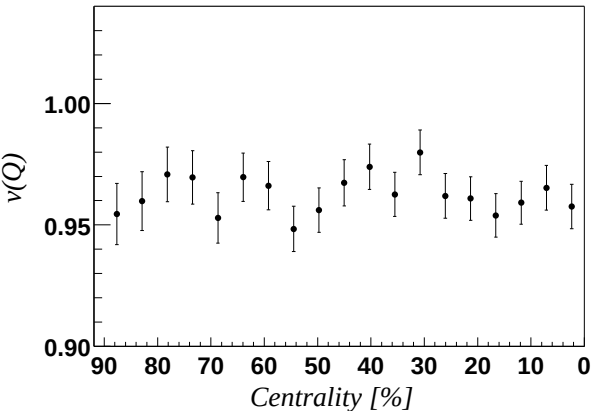

Figure 3.2: $v(Q)$ as a function of centrality.

trality is divided into 20 classes, which are determined from the BBC and ZDC information as shown in figure 3.3. The rightmost data point in figure 3.2 corresponds to the 0-5% most central events. The magnitude of $v(Q)$ does not depend on centrality. For the 10% most central events, the value is $v(Q) = 0.965 \pm 0.007$. If the difference when applying (3.20) is taken to be a systematic error the result is

$$v(Q) = 0.965 \pm 0.007(\text{stat}) - 0.019(\text{syst}) \tag{3.38}$$

However not as drastic as was predicted with a QGP transition, there is a clear reduction compared to the expected value from equation (3.33). Taking the limited geometrical acceptance of the detector into account, the result is consistent with the resonance gas prediction mentioned on page 27. With larger acceptance the probability to detect both charged decay particles from neutral resonances increases. This is seen in figure 3.4, where $v(Q)$, for the 10% most central events, is displayed as a function of $\Delta\varphi_r$. (Here φ_r denotes the reconstructed azimuthal emission angle of a particle, and $\Delta\varphi_r$ defines the region where particles are accepted in the analysis, explained further by figure 3.5.) Above $\Delta\varphi_r$=40° the behavior of $v(Q)$ clearly deviates from what is expected solely from global charge conservation (the solid curve). Figure 3.4 also shows good qualitative agreement between the data and the RQMD simulation.

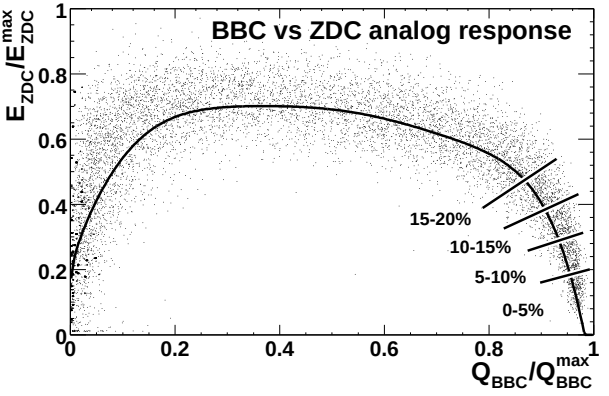

Figure 3.3: The centrality classes determined by the charge in the BBC and the energy in the ZDC.

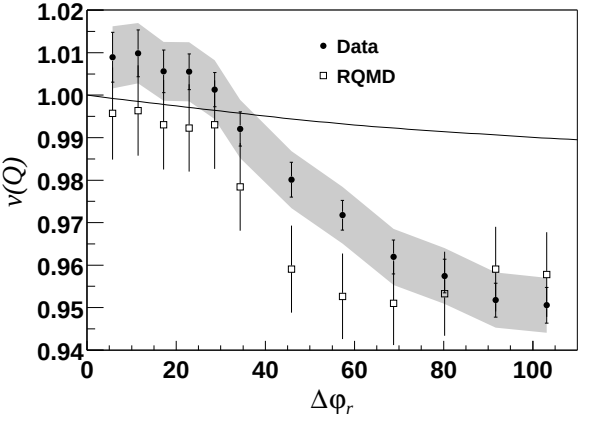

Figure 3.4: $v(Q)$ for the 10% most central events as a function of $\Delta\varphi_r$. For data, the error band shows the total statistical error, and the error bars the uncorrelated part.

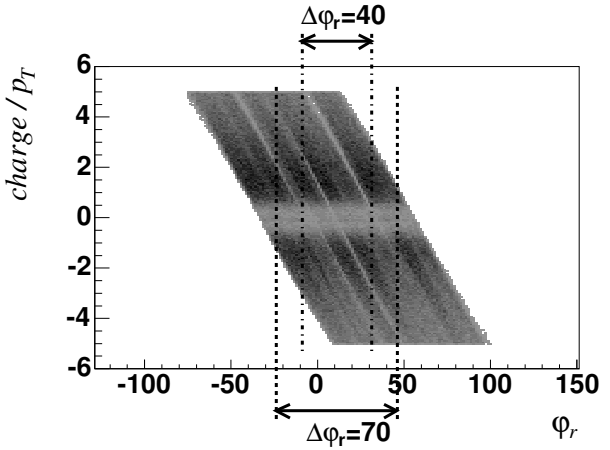

Figure 3.5: Charge/p_T vs. φ_r for a subset of the detected particles. $\Delta\varphi_r$ is chosen around the φ_r mid-point of the detector arm. As an illustration of this cut, two examples are shown here.

3.2.2 $\sqrt{s_{NN}}$ =200 GeV

The data from the second run period at RHIC were collected with a lot of improvements since the 130 GeV run. With higher event statistics, better detector performance, and higher quality track-definition, a more sensitive study of net-charge fluctuations became possible.

Event and Track Selection

When studying fluctuations in the number of particles, it is very important to have the detector operate under stable conditions, since average corrections are very difficult to apply. The event sample used in this analysis was therefore very carefully selected. It contains about 850,000 minimum bias events.

It is of course desirable to have a narrow distribution of z vertex position and high quality of tracks through the detector. Still, to perform a fluctuation analysis, high statistics is required, both in the number of events and in the number of tracks for each event. In this analysis the fluctuation measurement did not show any sensitivity to changes in the cut on z vertex position, and the cut of $|z| < 17$ cm was used, as in the 130 GeV analysis. The p_T cut used here was $0.2 < p_T < 2$ GeV/c. As will be shown from the Hijing simulations (figure 3.15) the background increases near the low and high end of this range.

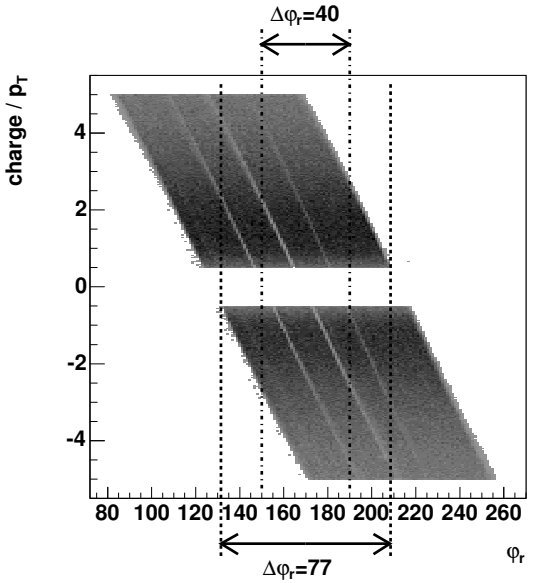

Figure 3.6: Charge/p_T vs. φ_r for a subset of the detected particles. $\Delta\varphi_r$ is chosen around the φ_r mid-point of the detector arm. As an illustration of this cut, two examples are shown here.

In the attempt to reveal dynamical correlations it is important to study how the net-charge fluctuation measure varies with acceptance. For this purpose cuts were made on pseudo-rapidity and on the φ_r angle, i.e. the reconstructed angle from the interaction vertex. To make cuts for the latter case a $\Delta\varphi_r$ window was defined in the same way as in section 3.2.1, further explained by figure 3.6. As can be seen in this figure, there is a breaking point at $\Delta\varphi_r \approx 77°$. Extending $\Delta\varphi_r$ above this value changes the acceptance in a complicated way. The maximum $\Delta\varphi_r$ used when showing the results later on is therefore close to this value.

The analysis was done in the east tracking arm, due to better detector performance of the drift chamber compared to the west arm. Three different levels of track matching cuts were applied. The first is referred to as "dc+pc1" in the figures. The tracks passing this cut are based on the information from the drift chamber and the first pad chamber plane. No requirements on track matching with other detectors are made. The second, referred to as "dc+pc1+pc3", utilizes a track matching cut where tracks are accepted if the distance between the projected and the actual PC3 hit is within three standard deviations of the PC3 position resolution. In the third cut, "dc+pc1+(pc3||emc)", tracks are accepted if they are matched to a PC3 *or* to an EMC hit, also within three

standard deviations. The third cut was introduced with the inefficient areas of PC3 east in mind, since these areas could potentially affect positive and negative particles with the same φ_r differently.

Ghost tracks arising in the drift chamber could severely affect the analysis. Figure 3.7 shows the distribution of $\Delta\varphi_{DC}$ and Δzed for pairs of nearby tracks. $\Delta\varphi_{DC}$ is the difference in azimuthal angle at the drift chamber reference radius,

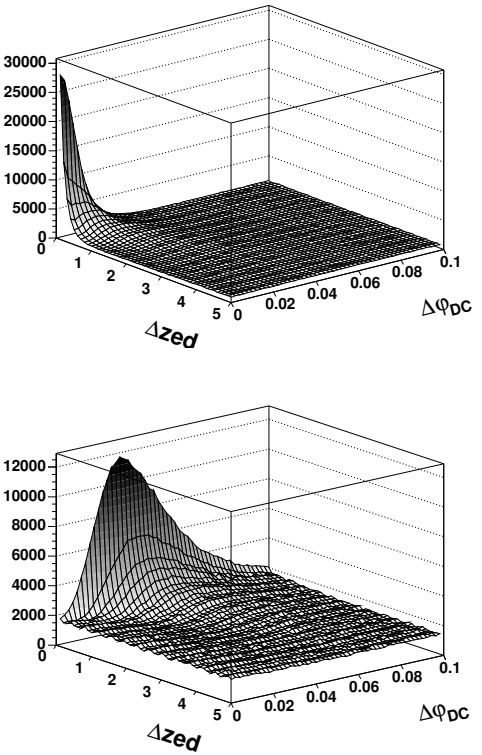

Figure 3.7: Number of track pairs with $\Delta\varphi_{DC} < 0.1$ rad and $\Delta zed < 5$ cm, shown for:
Two positively charged tracks (top).
One positively and one negatively charged track (bottom).
The distribution for two negatively charged tracks is similar to the first case.

and Δzed is the longitudinal distance, also at the drift chamber, between the tracks. One of the tracks from pairs showing up in the peaks should be a ghost. When considering only like sign pairs it could be argued that only one of the

tracks should be rejected, especially if the two tracks get roughly the same p_T. For unlike sign pairs it is however difficult to choose between the tracks, and to be consistent, both tracks are removed in all three cases ($++, +-$, and $--$). The cut is set at $\Delta\varphi_{DC} < 0.02$ rad and $\Delta zed < 1$ cm for the like sign pairs. For unlike sign pairs the distribution of the ghost peak seen in the bottom diagram of figure 3.7 gets narrower if our track sample is divided into smaller p_T windows. In figure 3.8 it is shown that the peak position in $\Delta\varphi_{DC}$ of this

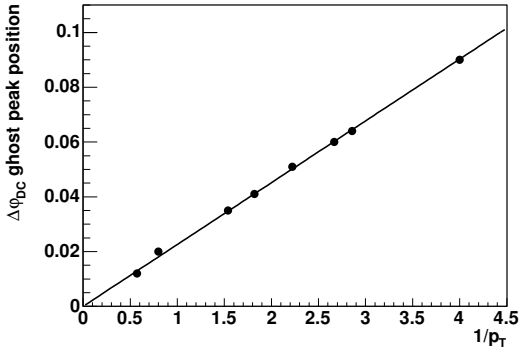

Figure 3.8: Peak position in $\Delta\varphi_{DC}$ of the unlike sign pairs as a function of $1/p_T$. The straight line fit shows the proportionality.

distribution is proportional to $1/p_T$. To be exact, the cut used is

$$|\Delta\varphi_{DC} - 0.0258/\overline{p_T}| < 0.02\text{rad} \qquad , \qquad \Delta zed < 1\text{cm} \tag{3.39}$$

where $\overline{p_T}$ is the mean value of the transverse momentum of the two tracks. To quantify the ghosting effect, the tracks from data are compared with tracks from mixed events. The difference of the number of tracks that fall into the $\Delta\varphi_{DC}$ and Δzed window defined by the boundaries of figure 3.7, i.e. $\Delta zed < 5$ cm and $\Delta\varphi_{DC} < 0.1$ rad, is shown in figure 3.9 as the fraction of the total number of tracks in the events. With the ghost track cut the fraction of tracks with a non-accidental companion track is below 1%. It should be pointed out that in the end the fluctuation measurements are not affected very much by this ghost track cut.

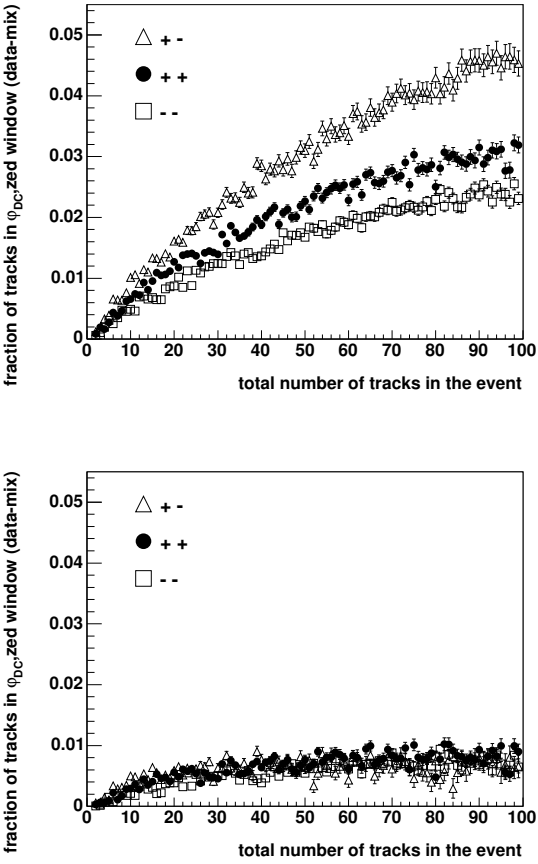

Figure 3.9: Top diagram shows the fraction of the difference between the number of tracks falling inside Δzed <5 cm and $\Delta\varphi_{DC}$ <0.1 rad in data and in mixed events. In the bottom diagram the ghost track cut has been applied.

The centrality selection is based on the BBC and ZDC information, as illustrated in figure 3.10. The n_{ch} distributions for some centrality classes are

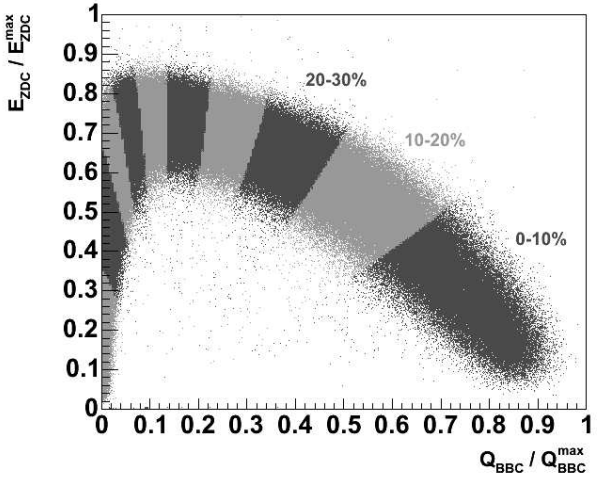

Figure 3.10: ZDC energy vs. BBC charge for different centrality classes.

shown for the "dc+pc1" case in figure 3.11.

In figure 3.12 the Q distributions are shown for the "dc+pc1" and the "dc+pc1+pc3" cases. The additional, positively charged background due to secondary interactions gives rise to a positive charge asymmetry, ε, in the first case. Since much of this background is removed when requiring association to PC3, ε is almost zero in the second case. Actually, some positive net charge is expected due to the net baryon number. BRAHMS has determined the net proton number to be $dN_p/dy \approx 6$ for central events [41]. In the one arm PHENIX acceptance this corresponds to $\langle Q \rangle \approx 6 \cdot 0.7 \cdot 0.25 \approx 1$, disregarding the limited p_T acceptance and detector inefficiencies.

In figure 3.13 $\langle Q \rangle$ is shown as a function of $\langle n_{ch} \rangle$ for different centrality classes and matching cuts. In all three cases there is an approximate straight line dependence, showing that ε is independent of centrality. Straight line fits yield the values 0.089, -0.006, and -0.026. The slightly negative ε when using EMC is due to the higher efficiency for annihilating anti-protons than protons.

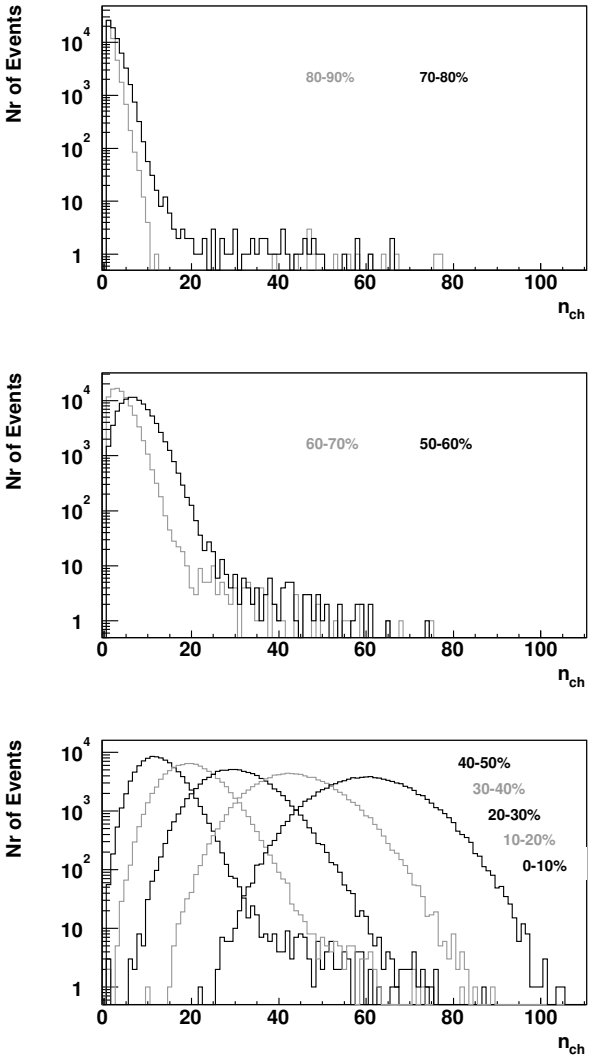

Figure 3.11: Distribution of n_{ch} for different centrality classes. ($\Delta\varphi_r = 75°$ is used.)

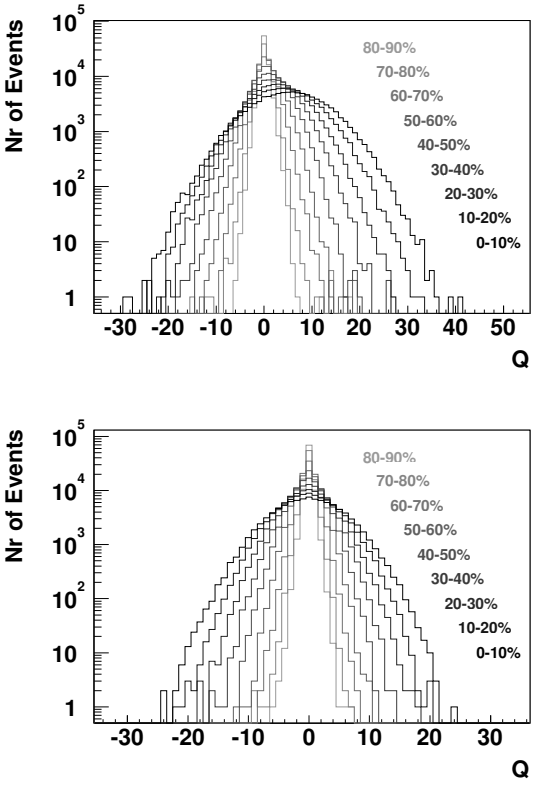

Figure 3.12: Distribution of net charge, Q, for different centrality classes. The top panel shows the dc+pc1 requirement and the bottom panel is for the dc+pc1+pc3 cut. ($\Delta\varphi_r = 75°$ is used.)

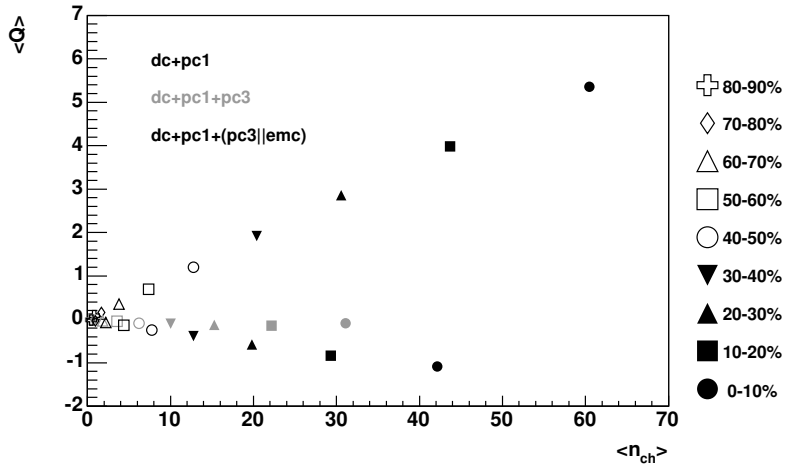

Figure 3.13: $\langle Q \rangle$ vs. $\langle n_{ch} \rangle$ for different matching cuts and centrality classes.

Detector Response Simulations Using Hijing

In order to study some detector effects, a sample of about 17,000 central Hijing events was processed through PISA. Simulating the detector response, effects of detector efficiency, background, and the acceptance fraction, p_a, could be estimated. For $0.2 < p_T < 2$ GeV, p_a was measured to be p_a=0.021. To a first approximation, this value should not change significantly with centrality.

The reconstruction efficiency has been estimated by studying particles originating from the primary vertex, traversing DC and PC1. Particles with reconstructed p_T within three standard deviations of the p_T resolution (shown in figure 3.14) and with correct charge are considered to be reconstructed. The result is shown in figure 3.15. Here the slightly smaller geometrical acceptance when associating tracks to PC3 and EMC has not been taken into account. This is instead regarded as an inefficiency.

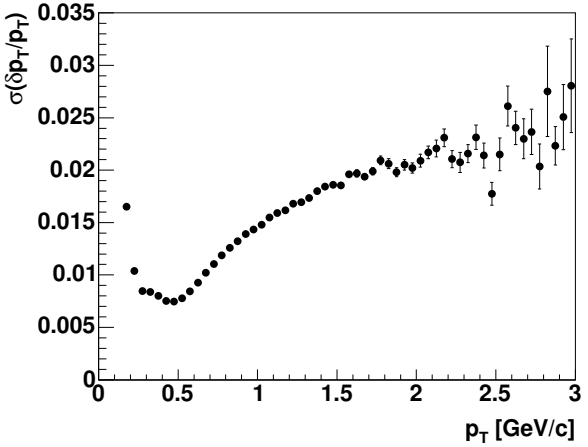

Figure 3.14: Resolution in p_T.

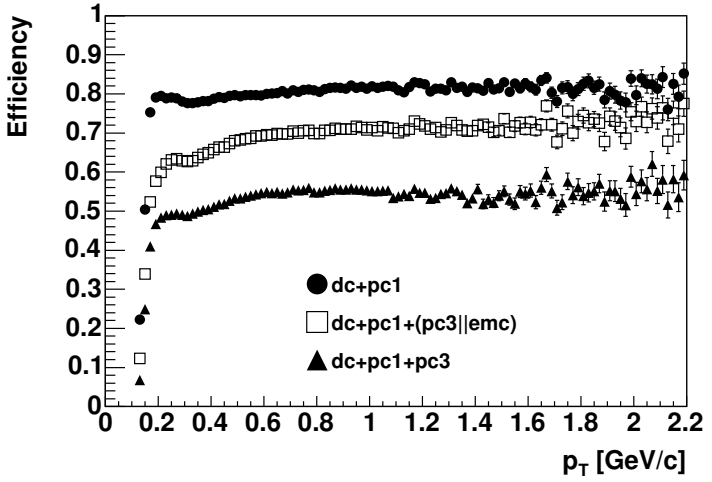

Figure 3.15: Efficiency vs. p_T. The mean values for $0.2 < p_T < 2$ GeV are
dc+pc1: 79.4%
dc+pc1+(pc3||emc): 66.4%
dc+pc1+pc3: 51.9%.

The background contribution was estimated in the following way. If the detected particle originates from the primary vertex itself, it is considered part of the background if the reconstructed charge is different from that of the generated particle. For secondaries, all reconstructed particles originating from the same primary particle are studied. If their net charge is different from that of the primary particle, they are considered part of the background. The background contribution is shown as a function of reconstructed p_T in figure 3.16. A large contribution to the background comes from interactions in detector

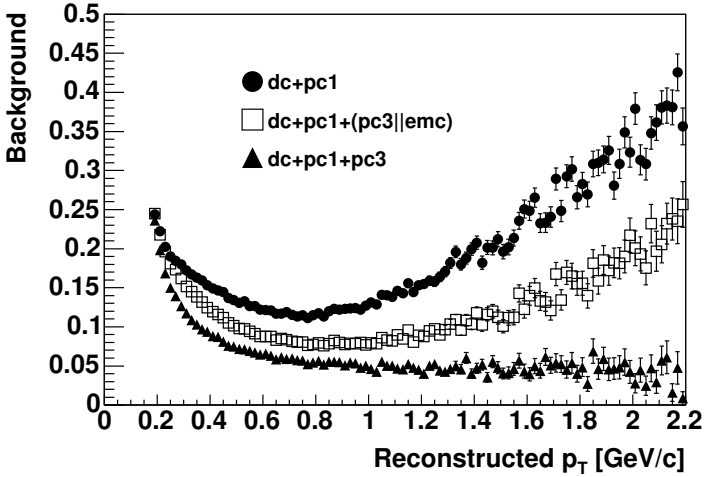

Figure 3.16: Estimated background vs. reconstructed p_T.
The mean values for $0.2 < p_T < 2$ GeV are
dc+pc1: 16.0%
dc+pc1+(pc3||emc): 13.2%
dc+pc1+pc3: 10.1%.

materials. The rest comes from processes, such as $K^0 \to \pi^+\pi^-$, $\pi^0 \to e^+e^-$, $\Lambda \to p\pi$, and $\gamma \to e^+e^-$ where only one of the secondary particles is detected. $K^\pm \to \mu^\pm\nu$ also contributes to the background, but most often (in about 90-95% of the cases, depending on track matching cut) the muon is reconstructed with the same charge as the kaon. When requiring track association the amount of the background originating from interactions in detector material decreases. Since there is an excess of positive particles from these interactions, the ε value is higher for the "dc+pc1" case. The high occupancy and poorer position resolution in EMC makes it less powerful in suppressing the background tracks. The Hijing results on net-charge fluctuations are presented below together with

the results from data.

Results

In PAPER IV it is shown that if there is an asymmetry in the net-charge, $\varepsilon \equiv \langle Q \rangle / \langle n_{ch} \rangle \neq 0$, the Γ measure is more appropriate than $v(Q)$ for analyzing the fluctuations. The Γ measure was therefore used in this analysis.

The Γ measure as a function of $\Delta\varphi_r$ is presented in figures 3.17-3.19 for various centrality classes and track matching cuts. The results are also compared to the pure global charge conservation case, calculated from $\Gamma = (1-p_a)(1-\varepsilon^2)$, as derived in equation (3.29).

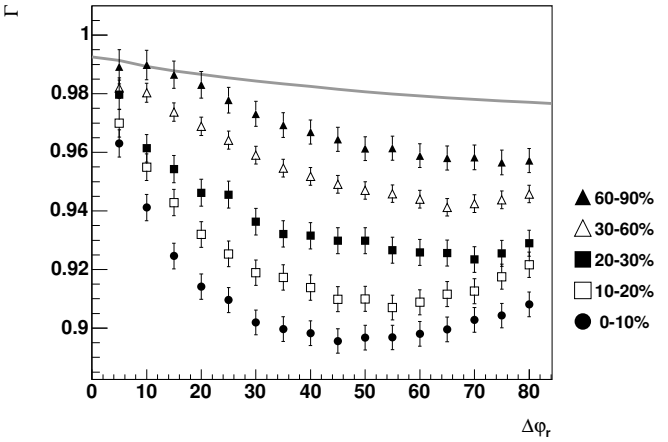

Figure 3.17: Γ as a function of $\Delta\varphi_r$ for various centrality classes, using the dc+pc1 matching cut. The solid curve shows the global charge conservation case.

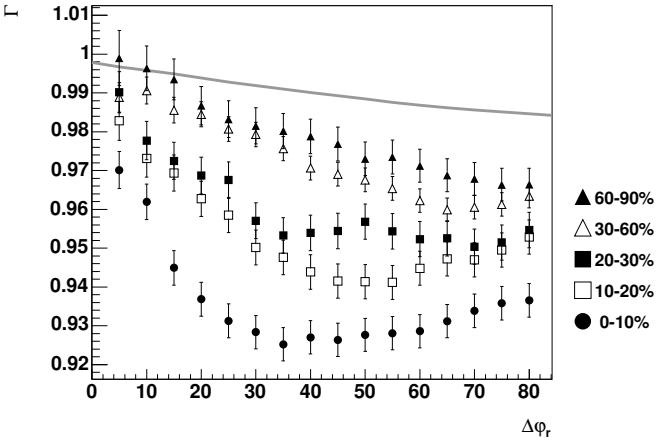

Figure 3.18: Γ as a function of $\Delta\varphi_r$ for various centrality classes, using the dc+pc1+pc3||emc matching cut. The solid curve shows the global charge conservation case.

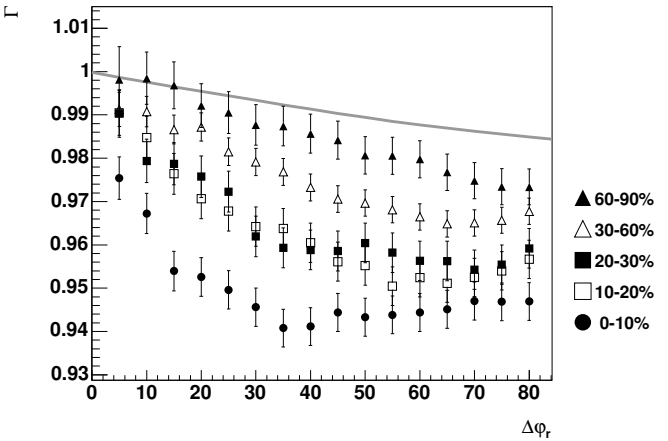

Figure 3.19: Γ as a function of $\Delta\varphi_r$ for various centrality classes, using the dc+pc1+pc3 matching cut. The solid curve shows the global charge conservation case.

The same trend is seen for all matching cuts. The net-charge fluctuations clearly decrease with centrality. To get a feeling for the quantitative significance of this decrease, the results will be compared to some model calculations below. Note that in these diagrams, for a given centrality class the points are correlated, since the data in one bin is a subset of the data in the next bin. The decrease is most notable in the vicinity of $\Delta\varphi_r = 50$.

Figure 3.20 shows the centrality dependence at this $\Delta\varphi_r$ cut for different matching cuts. The results are also compared to the simulations of central Hijing events. The difference in absolute values of Γ between the matching

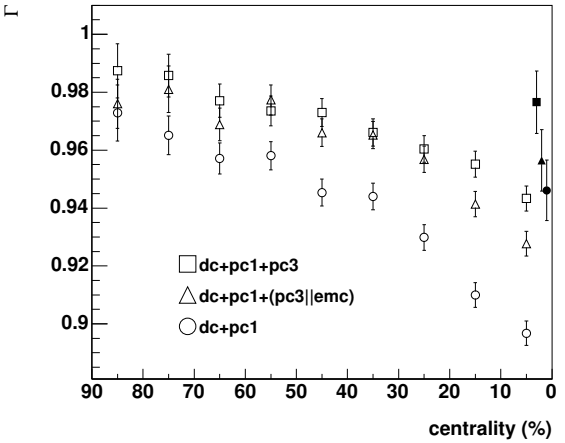

Figure 3.20: Γ as a function of centrality at $\Delta\varphi_r = 50$. The filled points show the simulation results.

cuts can be explained by the difference in efficiency known from the simulations. This is seen when introducing a slightly modified Γ measure. With the definition

$$\Gamma' \equiv \frac{1 - \frac{1-\Gamma}{p_e}}{1 - \varepsilon^2} \quad , \tag{3.40}$$

the efficiency and also the charge asymmetry dependence is removed. Figure 3.21 shows a good agreement between the various matching cuts when using Γ'.

The error bars in figures 3.17-3.19 only show the statistical error. To get a feeling for the systematic error a diagram of Γ at $\Delta\varphi_r = 50^\circ$ for subsets of the events, is shown in figure 3.22.

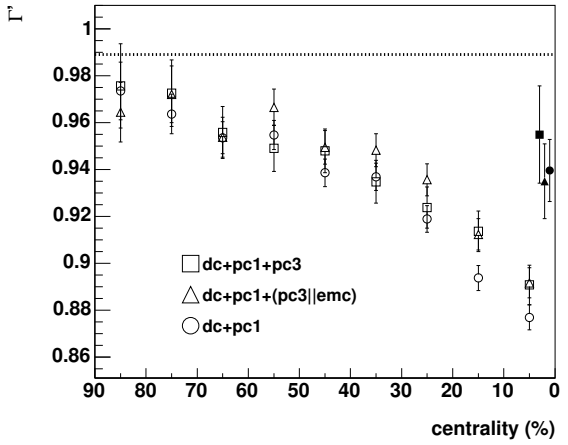

Figure 3.21: Γ' *as a function of centrality at* $\Delta\varphi_r = 50$. *The filled points show the simulation results. The dotted line shows the* $1 - p_a$ *value.*

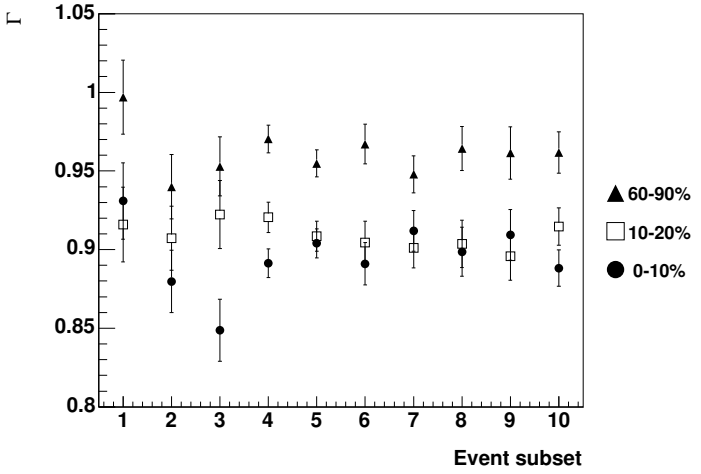

Figure 3.22: Γ *at* $\Delta\varphi_r = 50^\circ$ *for the "dc+pc1" case, for different run files and centrality selections.*

In figures 3.23-3.25 Γ is instead plotted against a pseudo-rapidity window of varying size, denoted $\Delta\eta$. These diagrams are made at $\Delta\varphi_r = 75°$.

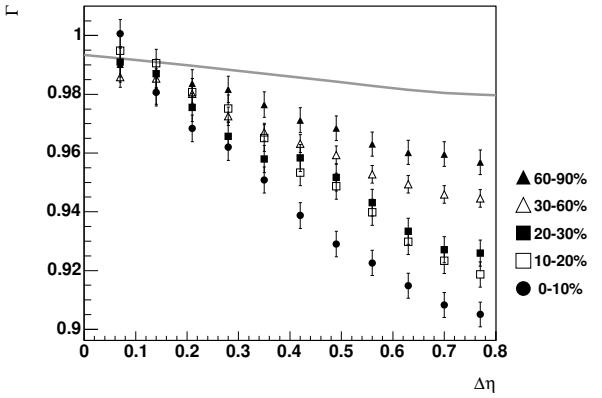

Figure 3.23: Γ as a function of $\Delta\eta$ for various centrality classes, using the dc+pc1 matching cut. The solid curve shows the global charge conservation case.

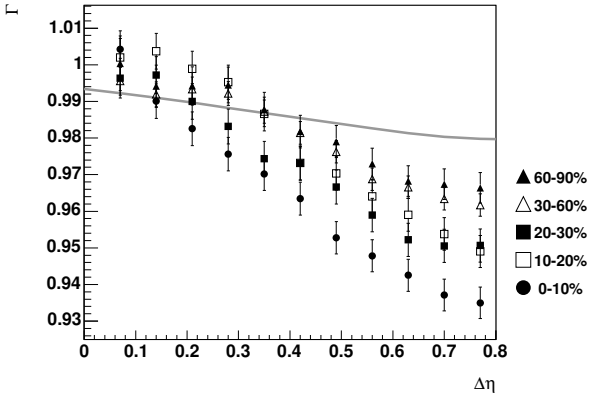

Figure 3.24: Γ as a function of $\Delta\eta$ for various centrality classes, using the dc+pc1+(pc3||emc) matching cut. The solid curve shows the global charge conservation case.

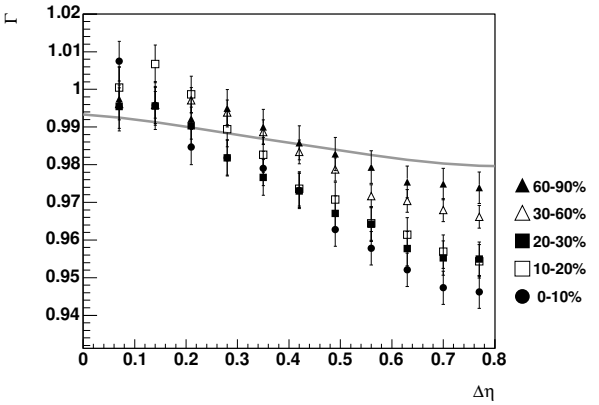

Figure 3.25: Γ as a function of Δη for various centrality classes, using the dc+pc1+pc3 matching cut. The solid curve shows the global charge conservation case.

The same decreasing trend is seen in these diagrams. Note that $\Delta\eta = 0.7$ corresponds to about $\Delta\theta_r = 40°$, which is close to the point where the magnitude of the net-charge fluctuations has a minimum in the case of the azimuthal angle ($\Delta\varphi_r$).

Comparison to Model Calculations

In order to study the reduction of the net charge fluctuations further, simulations based on the models described in PAPER IV are performed. The pure global charge conservation scenario is studied under the influence of neutral resonance decays, and a toy model of hadronization from a quark-gluon plasma is tested. In this model the quark combinations $u\bar{u}$, $d\bar{d}$, $u\bar{d}$, and $d\bar{u}$ fragment into two pions or three pions with the probabilities 30% and 70% respectively. With this construct, a lower limit of $\Gamma = 5/18$ is set, corresponding to the QGP state fluctuations (see equation (3.4)). Angular spread of the produced pions and detector inefficiencies will increase the fluctuations from this value.

In the pure global charge conservation case particles are randomly distributed in azimuthal angle, ϕ. For the resonance decays, where a neutral particle decays into one positive and one negative particle, the decay products are assigned a ϕ value with a separation angle given by a Gaussian distribution. A similar technique is used in the QGP hadronization model with the main difference that there are sometimes three outgoing particles. The $\Delta\varphi_r$ dependence of the two models should therefore be similar.

The main additions in the simulations, compared to the models in PAPER IV, are changes of the detector geometry and inclusion of a magnetic field, for applicability to PHENIX. Some parameters in these models are set, based on information from data and simulations. The mean value of the efficiency determined from the Hijing simulations is, for simplicity, used independently of p_T. Background tracks have only small influence on the fluctuations, why such tracks are omitted in these simulations. The p_T of the particles are exponentially distributed, and a flat distribution in pseudo-rapidity is used, in accordance with data.

In figure 3.26, 25% of the particles in each event are produced according to

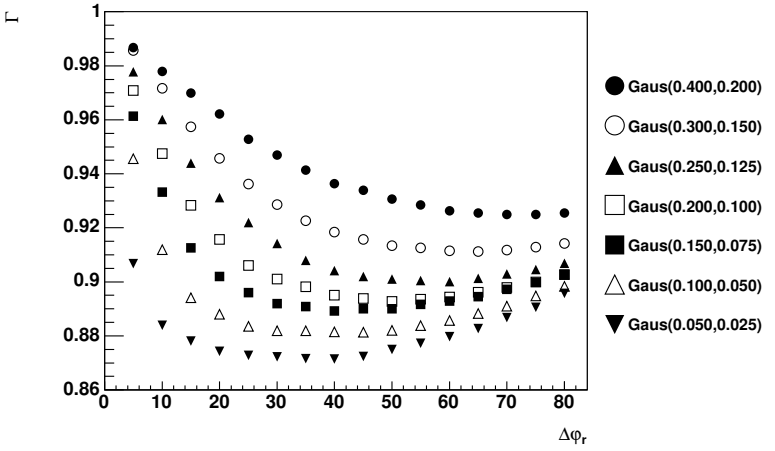

Figure 3.26: Γ vs. $\Delta\varphi_r$ for different distributions of angular separation between the generated pions in the QGP model.

the QGP hadronization model. This could also be interpreted as a mixture of events with QGP generation *only* with events with global charge conservation *only*. Here different distributions of separation angle between the pions are compared. The Gaus(0.2,0.1) graph, referring to a Gaussian with a mean value of 0.2 radians and a standard deviation of 0.1 radians, best fits the shape seen in the most central events in data and is therefore used in figure 3.27. Here, Γ is shown as a function of $\Delta\varphi_r$ for different fractions of QGP generated particles in each event. This figure also presents a direct comparison to the data from figure 3.17.

This is an extraordinary result, showing that this simple QGP hadronization model presents a good qualitative description of the data. A similar result is obtained from the resonance decay model, which is shown in figure 3.28. The

same Gaussian distribution for the separation angle was used here. The small difference between the models only slightly affects the shape of the resulting graphs. Even this model presents a good description of the data. However, resonance contributions are not expected to have any centrality dependence and the 25% admixture needed to account for the effect is probably unphysically large.

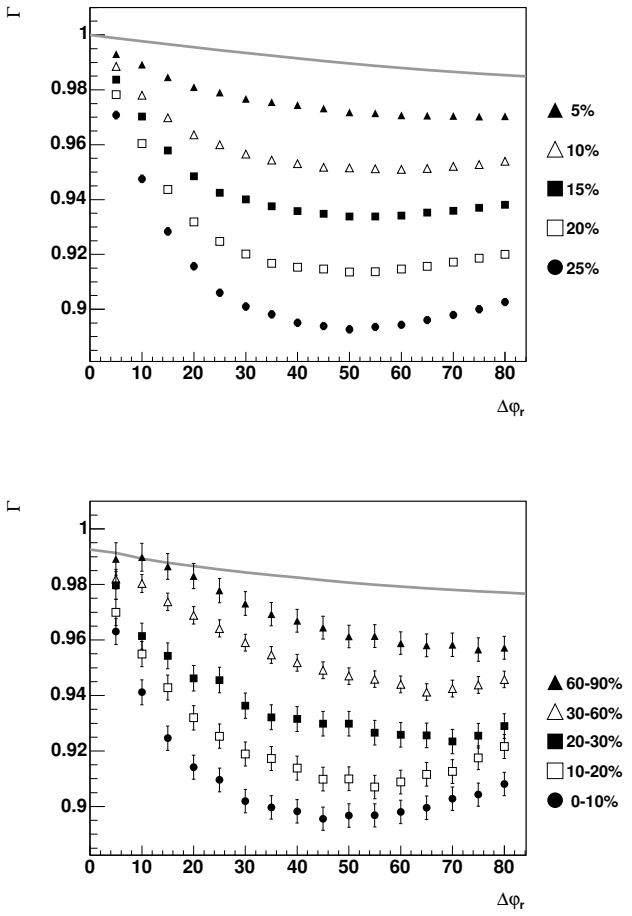

Figure 3.27: Γ *as a function of* $\Delta\varphi_r$ *for the QGP model (top) compared to data (bottom), using the "dc+pc1" cut. The percentages shown in the top diagram are the fraction of particles generated using the QGP model.*

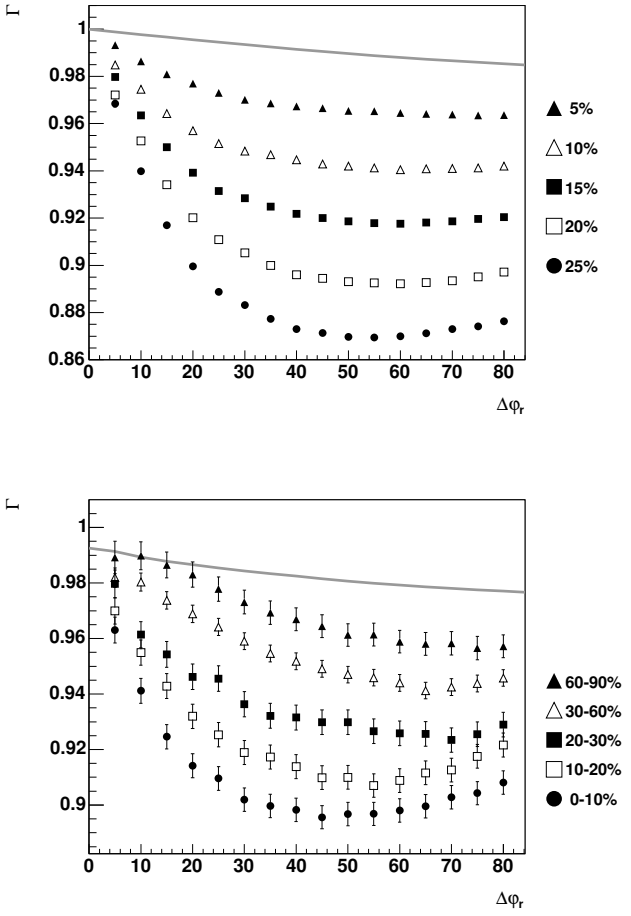

Figure 3.28: Γ as a function of $\Delta\varphi_r$ for the resonance decay model (top) compared to data (bottom), using the "dc+pc1" cut.

3.3 Conclusions

Since the proposal of reduced net-charge fluctuations as a signal for the creation of a deconfined phase, a lot of work has led to improvements in the analysis techniques, as well as development of more appropriate fluctuation measures. Results from various experiments indicate that the initial predictions on the reduced magnitude of the fluctuations probably were too optimistic. Still, very interesting observations have been made, and it is clear that analyses of this kind may give valuable information on the particle production mechanism.

The 130 A GeV analysis of net-charge fluctuations in PHENIX data shows no significant centrality dependence. Those measurements are consistent with the corresponding results from STAR [42]. The magnitude of the reduction of the fluctuations is comparable to what is found from different event generators.

In the 200 A GeV PHENIX data the fluctuations are further reduced, by a factor of two as compared to the Hijing simulations. That is, not all of this effect can be explained by resonance decays included in the simulations. As the quality of these data results in higher sensitivity to fluctuations, a centrality dependence is also revealed. Similar results are reported by STAR at 200 A GeV [43]. There is thus an increase of the strength of the correlation between positive and negative particles with event centrality. This can either be due to an increase in the number of correlated particles or to a stronger correlation between the correlated particles. The origin of this centrality dependence is unknown, but, as shown here, it is consistent with a simple QGP scenario.

At CERN SPS energies NA49 sees no significant centrality dependence of the fluctuations [44], whereas NA45 does not rule out such a possibility [45].

As the new 200 A GeV Au+Au data taken at RHIC in 2004 are about to be prepared for physics analyses, PHENIX can look forward to much higher statistics, probably taken under more stable conditions, since the rate of data taking has increased considerably since the previous run. With these improvements, further conclusions can hopefully be drawn.

Acknowledgments

I would like to express my gratitude to everyone at the division of experimental high-energy physics (as well as the former division of cosmic and subatomic physics) for all their help and support over the years. Especially I would like to thank:

Head of division and research group Hans-Åke Gustafsson, supervisors Anders Oskarsson and Evert Stenlund, for all their help and advice.

Joakim Nystrand, for introducing me to the analysis topic of net-charge fluctuations, and for all his help with the analysis work.

Former students Pål Nilsson, David Silvermyr, and Rickard du Rietz, for their help on various software issues. I enjoyed working with you.

Lennart Österman, for nice solutions to numerous computer and software related problems.

Graduate students Sarah Rosendahl and Eva Haslum, my new room mates Magnus Hansson, Albert Knutsson and Sakar Osman, who along with the other students at the division helped creating a friendly atmosphere.

I would also like to thank all the PHENIX collaborators who helped me with various practical stuff while at BNL. Special gratitude goes to Charles F. Maguire, for his quick and accurate responses to numerous questions on PHENIX software.

The financial support from NORDITA, Kungliga Fysiografiska Sällskapet i Lund, and the organizers of Quark Matter '02 is also gratefully acknowledged.

Finally I would like to thank family and friends for all their support throughout the years.

Bibliography

[1] G. Kane
Modern Elementary Particle Physics,
Addison-Wesley (1993)

[2] S. Eidelman *et al.* ,
Phys. Lett. B **592** (2004) 1

[3] J.D. Bjorken,
Phys. Rev. D **27** (1983) 140

[4] J.W. Harris, B. Müller,
Ann. Rev. Nucl. Part. Sci. **46** (1996) 71

[5] http://www.bnl.gov/RHIC

[6] http://www.phenix.bnl.gov

[7] G.D. Westfall et al.,
Phys. Rev. Lett. **37** (1976) 1202

[8] K. Adcox *et al.* (PHENIX Collaboration),
Phys. Rev. Lett. **88** (2002) 192302
S.S. Adler *et al.* (PHENIX Collaboration),
arXiv:nucl-ex/0401003, submitted to Phys. Rev. Lett.

[9] S.S. Adler *et al.* (PHENIX Collaboration),
arXiv:nucl-ex/0406004, submitted to Phys. Rev. Lett.

[10] E. Schnedermann, J. Sollfrank, U. Heinz,
Phys. Rev. C **48** (1993) 2462

[11] M. Gyulassy, M. Plümer,
Phys. Lett. B **243** (1990) 432

[12] X.N. Wang, M. Gyulassy,
Phys. Rev. Lett. **68** (1992) 1480

[13] K. Adcox *et al.* (PHENIX Collaboration),
Phys. Rev. Lett. **88** (2002) 022301

[14] K. Adcox *et al.* (PHENIX Collaboration),
Phys. Lett. B **561** (2003) 82

[15] S.S. Adler *et al.* (PHENIX Collaboration),
Phys. Rev. Lett. **91** (2003) 072303

[16] S.S. Adler *et al.* (PHENIX Collaboration),
Phys. Rev. C **69** (2004) 034910

[17] C. Adler *et al.* (STAR Collaboration),
Phys. Rev. Lett. **89** (2002) 202301

[18] J. Adams *et al.* (STAR Collaboration),
Phys. Rev. Lett. **91** (2003) 072304

[19] S.S. Adler *et al.* (PHENIX Collaboration),
Phys. Rev. Lett. **91** (2003) 182301

[20] J. Adams *et al.* (STAR Collaboration),
Phys. Rev. Lett. **92** (2004) 062301

[21] B.B. Back *et al.* (PHOBOS Collaboration),
arXiv:nucl-ex/0407012, submitted to Phys. Rev. C

[22] F. Retière,
J. Phys. G **30** (2004) S827

[23] J. Rafelski, B. Müller,
Phys. Rev. Lett. **48** (1982) 1066

[24] E. Andersen *et al.* (WA97 Collaboration),
Phys. Lett. B **449** (1999) 401

[25] T. Matsui, H. Satz,
Phys. Lett. B **178** (1986) 416

[26] M.C. Abreau *et al.* (NA50 Collaboration),
Phys. Lett. B **477** (2000) 28

[27] S.S. Adler *et al.* (PHENIX Collaboration),
Phys. Rev. C **69** (2004) 014901

[28] D. Lissauer, E.V. Shuryak,
Phys. Lett. B **253** (1991) 15

[29] D. Mukhopadhyay (for the PHENIX Collaboration),
Nucl. Phys. A **715** (2003) 494c

[30] F. Steffen, M. Thoma,
Phys. Lett. B **510** (2001) 98

[31] J. Frantz (for the PHENIX Collaboration),
J. Phys. G **30** (2004) S1003

[32] H. Heiselberg, A. D. Jackson,
Phys. Rev. C **63** (2001) 064904

[33] S. Jeon and V. Koch,
Phys. Rev. Lett. **85** (2000) 2076

[34] M. Asakawa, U. Heinz, B. Müller,
Phys. Rev. Lett. **85** (2000) 2072

[35] D.P. Morrison *et al.* (PHENIX Collaboration),
Nucl. Phys. A **638** (1998) 565

[36] H. Sorge,
Phys. Rev. C **52** (1995) 3291

[37] X.N. Wang, M. Gyulassy
Phys. Rev. D **44** (1991) 3501
M. Gyulassy, X.N. Wang
Comput. Phys. Commun. **83** (1994) 307

[38] R. Brun, F. Carminati,
"GEANT Detector Description and Simulation Tool"
CERN Program Library Long Writeup W5013

[39] S. Mrówczyński,
Phys. Rev. C **66** (2002) 024904

[40] C. Pruneau, S. Gavin, S. Voloshin,
Phys. Rev. C **66** (2002) 044904

[41] I.G. Bearden *et al.* (BRAHMS Collaboration),
arXiv:nucl-ex/0312023, submitted to Phys. Rev. Lett.

[42] J. Adams *et al.* (STAR Collaboration),
Phys. Rev. C **68** (2003) 044905

[43] G.D. Westfall (for the STAR Collaboration),
J. Phys. G **30** (2004) S1389

[44] C. Alt *et al.* (NA49 Collaboration),
arXiv:nucl-ex/0406013

[45] H. Sako, H. Appelshäuser (for the NA45 Collaboration),
J. Phys. G **30** (2004) S1371